

# Applications of Deep Learning to Ocean Data Inference and Sub-Grid Parameterisation

[Note: This is a non-peer reviewed preprint submitted to EarthArXiv. The manuscript has been submitted to the Journal of Advances in Modeling Earth Systems (JAMES) for peer review.]

Thomas Bolton<sup>1</sup>, Laure Zanna<sup>1</sup>

<sup>1</sup>Department of Physics, University of Oxford, UK.

## Key Points:

- We successfully use convolutional neural networks to predict unresolved turbulent processes and sub-surface velocities.
- The neural networks generalise to different regions and model configurations.
- Global momentum conservation can be respected without sacrificing accuracy.

---

Corresponding author: Thomas Bolton, [tom.bolton@physics.ox.ac.uk](mailto:tom.bolton@physics.ox.ac.uk)

**Abstract**

Oceanographic observations are limited by sampling rates, while ocean models are limited by finite resolution and high viscosity and diffusion coefficients. Therefore both data from observations and ocean models lack information at small-scales. Methods are needed to either extract information, extrapolate, or up-scale existing oceanographic datasets, to account for the unresolved physical processes. Here we use machine learning to leverage observations and model data by predicting unresolved turbulent processes and sub-surface flow fields. As a proof-of-concept, we train convolutional neural networks on degraded-data from a high-resolution quasi-geostrophic ocean model. We demonstrate that convolutional neural networks successfully replicate the spatio-temporal variability of the sub-grid eddy momentum forcing, are capable of generalising to a range of dynamical behaviours, and can be forced to respect global momentum conservation. The training data of our convolutional neural networks can be sub-sampled to 10-20% of the original size without a significant increase in accuracy. We also show that the sub-surface flow field can be predicted using only information at the surface, mimicing when only satellite altimetry data is available. Our study indicates that data-driven approaches can be exploited while respecting physical principles, even when data is limited to a particular region or external forcing.

**1 Introduction**

Satellite observations have produced a wealth of information on the ocean circulation [Morrow *et al.*, 1994; Le Traon and Morrow, 2001; Scott and Wang, 2005; Chelton *et al.*, 2007; Greatbatch *et al.*, 2010b; Abernathey and Marshall, 2013]. However raw satellite altimetry data sub-samples the ocean, and does not measure sub-surface quantities. Temporally measurements at the same location are made twice every orbital cycle, while the spatial sampling depends upon the distance between ground tracks. To improve the sub-sampling rates, measurements from multiple satellites are combined [Le Traon *et al.*, 1998] to produce an optimal estimate.

The process of combining measurements from multiple satellites includes spatio-temporal filtering, which leads to a more ‘smoothed’ view of the dynamical processes at the oceans surface, removing variability due to mesoscale and sub-mesoscale eddies. The filtering can also lead to spurious physical signals, as studied by Arbic *et al.* [2013], which showed that filtering data can lead to exaggerated forward-cascades of energy. The new Surface Water and Ocean Topography (SWOT) mission will have a large swath of 120 km, providing unprecedented detail on the oceans surface. Despite the high spatial sampling rate, measurements may still be limited by the temporal sampling rate of 11 days [Durand *et al.*, 2010].

Similar to satellite observations, Ocean General Circulation Models (OGCM) are useful for studying ocean dynamics. However, high-resolution models are computationally expensive, and the current resolution of models is not high enough to fully resolve the first baroclinic deformation radius at mid-latitudes [Hallberg, 2013]. Also, due to their finite resolution, they require large viscosity and diffusion coefficients in order to remain numerically stable [Jochum *et al.*, 2008]. The combination of finite-resolution and artificially high viscosity, diffuses momentum and smooths out features such as jets and mesoscale eddies [Hewitt *et al.*, 2016; Kjellsson and Zanna, 2017].

Therefore both observations and models are missing the interactions of oceanic turbulence at small-scales, which play an important role in maintaining the large-scale circulation [Greatbatch *et al.*, 2010a,b; Waterman and Jayne, 2010; Waterman *et al.*, 2011; Kang and Curchitser, 2015]; with satellite observations only providing surface information. We thus consider the general problem: given some smoothed view of the oceans surface, what information can be generated on small-scale turbulent interactions and sub-surface quantities. Illuminating unresolved quantities using ‘seen’ quantities would ex-

65 tend the reach of existing datasets, and could potentially improve the representations  
66 of unresolved eddies in OGCMs.

67 We tackle this problem with machine learning. Machine learning has grown in pop-  
68 ularity in recent years, and has been applied to weather prediction [*McGovern et al.*, 2017;  
69 *Esteves et al.*, 2018], climate model parameter sensitivity studies [*Anderson and Lucas*,  
70 2018], chaotic dynamical systems forecasting [*Pathak et al.*, 2018a,b; *Vlachas et al.*, 2018],  
71 and parameterising unresolved atmospheric processes [*Gentine et al.*, 2018; *Brenowitz*  
72 *and Bretherton*, 2018; *Jiang et al.*, 2018; *O’Gorman and Dwyer*, 2018]. The foundational  
73 principle of machine learning is extracting information from data. When used to improve  
74 our understanding of the earth system, these data-driven methods are an empirical bottom-  
75 up approach, whereas the rationalist top-down approach considers physical principles  
76 and mechanisms. Here we take the empirical route by exploiting recent developments  
77 in machine learning.

78 Using empirical methods to leverage ocean observations is not new. For example,  
79 using satellite altimetry data, *Keating et al.* [2012] constructed a stochastic model to ‘super-  
80 resolve’ the velocity field and predict the velocity at depth. Similarly, *Keating and Smith*  
81 [2015] used a stochastic model to produce a super-resolved sea-surface temperature (SST)  
82 field, given a low-resolution observation of SST. With regards to machine learning, *Chap-*  
83 *man and Charantonis* [2017] constructed a form of neural network known as a self-organising  
84 map to reconstruct sub-surface velocities in the Southern ocean using satellite altime-  
85 try data and Argo floats. Other studies have used random forests to predict sub-surface  
86 temperature anomalies [*Su et al.*, 2018] and Southern Ocean oxygen content [*Giglio et al.*,  
87 2018].

88 In the previous studies that leverage oceanic observations, there is an abundance  
89 of coarse-resolution data (satellite altimetry), but limited data on the desired quantities  
90 (e.g high-resolution SST or Argo sub-surface velocities); as is the case with OGCMs, where  
91 high-resolution data is less readily available due to the computational cost. A similar chal-  
92 lenge is when data is only available for particular regions, such as mooring data [*Hogg*,  
93 1992] or gliders [*Rudnick et al.*, 2004; *Davis et al.*, 2008]. A machine learning algorithm  
94 trained on region-limited data would have to adapt to new regions with different physics;  
95 this task is well suited to a deep neural networks, which are known for a strong ability  
96 to generalise [*Krizhevsky et al.*, 2012; *LeCun et al.*, 2015; *Goodfellow et al.*, 2016].

97 However, deep neural networks are typically considered a ‘black box’, i.e., they lack  
98 simple interpretations. It is therefore difficult to assess whether such data-driven meth-  
99 ods respect physical principles (e.g. conservation of energy or momentum). For exam-  
100 ple, neural networks have been used to develop Reynolds-averaged turbulence models  
101 [*Tracey et al.*, 2015; *Kutz*, 2017], where the studies of *Ling et al.* [2016a,b] in particu-  
102 lar show that a neural network can respect Galilean invariance by utilising the invari-  
103 ant tensors of *Pope* [1975]. The studies of *Ling et al.* [2016a,b] are important in mov-  
104 ing towards data-driven approaches that respect the physical properties of the system.

105 In this paper we focus on a particular machine learning algorithm, namely convo-  
106 lutional neural networks, in order to leverage observations and coarse-resolution model  
107 data. Our aim is to test whether they can be used to reveal information on unresolved  
108 turbulent processes and sub-surface flow fields, and to determine if they are suited to sit-  
109 uations where data is limited to a particular region. To move towards these aims, as a  
110 proof-of-concept we will address the following questions:

- 111 1. Can convolutional neural networks represent the spatio-temporal variability of the  
112 sub-grid eddy momentum forcing.
- 113 2. How sensitive are the neural networks to the physical processes occurring within  
114 each region, and how well do they generalise to ocean models in different config-  
115 urations.

- 116 3. Is it possible to physically-constrain neural networks to respect global momentum  
 117 conservation.  
 118 4. Using only information at the surface, can neural networks predict the sub-surface  
 119 flow fields.

120 By using data from an idealised high-resolution ocean model, we show that con-  
 121 volutional neural networks can represent both the spatial and temporal variability of the  
 122 eddy momentum forcing. The region the neural network is trained on, and therefore the  
 123 dynamical processes occurring within that region, significantly impact the performance  
 124 of the neural network. In particular, training on the most turbulent region produces the  
 125 best overall performing neural network. The neural networks successfully generalise to  
 126 models with different viscosity coefficients and external wind forcings. Initially momen-  
 127 tum is not conserved globally, but the neural networks can be constrained to respect mo-  
 128 mentum conservation without a significant reduction in accuracy. A neural network can  
 129 accurately predict the sub-surface flow field when there is a strong barotropic compo-  
 130 nent to the flow.

131 The paper is organised as follows. The quasi-geostrophic ocean model, the degrad-  
 132 ing of model data, and convolutional neural network, are introduced in Section 2. Per-  
 133 formance diagnostics of the neural networks, in terms of non-local predictions and gen-  
 134 eralising to different model configurations, are presented in Section 3. We explore meth-  
 135 ods of physically-constraining the neural networks in Section 5. Section 6 presents a neu-  
 136 ral network trained to predict sub-surface flow fields using only information at the sur-  
 137 face. We summarise and discuss our results in Section 7.

## 138 2 Data and Methods

### 139 2.1 Quasi-Geostrophic Ocean Model

140 We use the PEQUOD model which solves the three-dimensional baroclinic quasi-  
 141 geostrophic (QG) potential vorticity equation, with constant wind forcing on a beta plane  
 142 [e.g. *Berloff, 2005*]. The model has a bounded-square domain with a flat bottom.

143 The configuration of this model leads to two large-scale circulation gyres separated  
 144 latitudinally by a strong meandering zonal jet. The model is configured to represent an  
 145 idealised version of current systems such as the Gulf Stream in the North Atlantic or the  
 146 Kuroshio Extension in the North Pacific; both these current systems exhibit vigorous  
 147 eddies interacting with a strong mean-flow. The time-mean streamfunction, which illus-  
 148 trates the double-gyre flow structure, can be seen in Figure 1a of *Mana and Zanna [2014]*.

149 The potential vorticity  $q$  is given by

$$q = \nabla^2 q + \beta y + \frac{\partial}{\partial z} \left( \frac{f_0^2}{N^2} \frac{\partial \psi}{\partial z} \right), \quad (1)$$

150 where  $f = f_0 + \beta y$  is the planetary vorticity,  $f_0$  is the Coriolis parameter,  $\beta =$   
 151  $df/dy$  is the Rossby parameter,  $\nabla = (\partial/\partial x, \partial/\partial y)$  is the horizontal gradient operator,  
 152  $N = \left(-\frac{g}{\rho} \frac{d\rho}{dz}\right)^{\frac{1}{2}}$  is the Brunt-Väisälä frequency,  $g$  is gravity,  $\rho$  is density, and  $\psi$  is the  
 153 streamfunction for the non-divergent horizontal velocity  $\mathbf{u} = (-\partial\psi/\partial y, \partial\psi/\partial x)$ .

154 The model has three layers ( $m = 1$  upper,  $m = 2$  middle,  $m = 3$  upper), with  
 155 thicknesses  $H_m$  of 250 m, 750 m, 3000 m, respectively. For each layer, the following prog-  
 156 nostic equation is solved

$$\frac{\partial q}{\partial t} + (\mathbf{u} \cdot \nabla)q = \mathcal{D} + \mathcal{F}, \quad (2)$$

157 where  $\mathcal{D} = \nu \nabla^4 \psi - r \nabla^2 \psi \delta_{m,3}$  is the dissipation, and  $\mathcal{F} = (\nabla \times \tau)_z \delta_{m,1} / \rho_0 H_1$  is  
 158 the applied wind stress curl forcing, where  $\delta_{i,j}$  is the Kronecker delta function. The hor-  
 159 izontal resolution of the model is 7.5 km, such that the model is eddy resolving. The first  
 160 term in the dissipation is a fourth-order term equivalent to Laplacian viscosity, with vis-  
 161 cosity coefficient  $\nu$ . The second dissipation term parameterises the presence of an Ek-  
 162 man layer with bottom drag coefficient  $r$  (and therefore only acts on the bottom  $m =$   
 163 3 layer). The wind stress forcing applied to the upper  $m = 1$  layer is given explicitly  
 164 by

$$\mathcal{F}(x, y) = \begin{cases} -\tau_0 \frac{0.92\pi}{L\rho_0 H_1} \sin\left(\frac{\pi y}{g(x)}\right) & y \leq g(x), \\ \tau_0 \frac{2\pi}{0.9L\rho_0 H_1} \sin\left(\frac{\pi[2y-g(x)]}{L-g(x)}\right) & y > g(x), \end{cases} \quad (3)$$

165 where  $g(x) = L/2 + 0.2(x - L/2)$ ,  $L = 3840$  km is the domain length, and  $\rho_0$  is  
 166 the reference density. After the model has been integrated from rest to a statistically steady  
 167 state, we save 10 years of model output at daily resolution of the turbulent double-gyre  
 168 circulation. For further details on the QG model, see *Mana and Zanna* [2014]; *Zanna*  
 169 *et al.* [2017], and for a list of the model parameters see Table 1. We use the data gener-  
 170 erated by the ocean model to train various neural networks, but only after degrading the  
 171 data, to make it similar to observations or low-resolution model.

## 172 2.2 Degrading High-Resolution Data

173 We degrade the fields from the high-resolution QG model using a spatial 2D low-  
 174 pass filter, in order to produce data that is similar to satellite altimetry or a model with  
 175 a large numerical dissipation. From the filtering of the model data, we can then calcu-  
 176 late the forcing from unresolved small-scale turbulent processes.

177 At every time slice in the data, we take a high-resolution variable  $a$  at a particu-  
 178 lar layer, and apply a two-dimensional spatial Gaussian filter. We denote filtered vari-  
 179 ables as  $\bar{a}$ , and sub-filter variables as the deviation from the filtered variable  $a' = a -$   
 180  $\bar{a}$ . The value of a function  $a(x, y)$ , after the Gaussian low-pass filtering operation  $G \star$   
 181  $a$  at a point  $(x_0, y_0)$ , is given by

$$\begin{aligned} \bar{a}(x_0, y_0) &= G \star a = \iint a(x, y) G(x_0, y_0, x, y) dx dy \\ &= \frac{1}{2\pi\sigma^2} \iint a(x, y) e^{-((x-x_0)^2 + (y-y_0)^2)/2\sigma^2} dx dy, \end{aligned} \quad (4)$$

182 where  $\sigma = 30$  km is the standard deviation of the Gaussian filter, which deter-  
 183 mines the length-scale at which information (below that length-scale) is removed. There-  
 184 fore the filter acts to remove information on dynamical processes at spatial scales smaller  
 185 than 30 km.

186 Using the low-pass filter defined in Equation 4, we can now express the effects of  
 187 the unresolved (sub-filter) variables onto the resolved (filtered) variables. Ignoring ver-  
 188 tical effects and planetary vorticity, the horizontal momentum equation is given by

$$\frac{\partial \mathbf{u}}{\partial t} + (\mathbf{u} \cdot \nabla) \mathbf{u} = \mathbf{F} + \mathbf{D}, \quad (5)$$

189 where  $\mathbf{F}$  and  $\mathbf{D}$  are the momentum forcing and dissipation, respectively. Apply-  
 190 ing a low-pass filter to Equation 5, and then adding  $(\bar{\mathbf{u}} \cdot \nabla) \bar{\mathbf{u}}$  to both sides of the equa-  
 191 tion, leads to

$$\frac{\partial \bar{\mathbf{u}}}{\partial t} + (\bar{\mathbf{u}} \cdot \nabla) \bar{\mathbf{u}} = \bar{\mathbf{F}} + \bar{\mathbf{D}} + [(\bar{\mathbf{u}} \cdot \nabla) \bar{\mathbf{u}} - \overline{(\mathbf{u} \cdot \nabla) \mathbf{u}}], \quad (6)$$

$$\frac{\partial \bar{\mathbf{u}}}{\partial t} + (\bar{\mathbf{u}} \cdot \nabla) \bar{\mathbf{u}} = \bar{\mathbf{F}} + \bar{\mathbf{D}} + \mathbf{S}, \quad (7)$$

$$\text{where } \mathbf{S} = \underbrace{(\bar{\mathbf{u}} \cdot \nabla) \bar{\mathbf{u}} - \overline{(\mathbf{u} \cdot \nabla) \mathbf{u}}}_{\text{Sub-filter eddy momentum forcing}}. \quad (8)$$

192 The low-pass filtering operation results in an additional forcing term in Equation 7  
 193 for the filtered momentum; the additional momentum forcing  $\mathbf{S}$  is given by Equation 8,  
 194 the divergence of a Reynolds stress. The vector  $\mathbf{S} = (S_x, S_y)$  represents the effects of  
 195 the sub-filter momentum field on the filtered momentum field, i.e., the interaction be-  
 196 tween small-scale eddies and the large-scale flow. As the sub-filter eddy forcing  $\mathbf{S}$  depends  
 197 on the sub-filter variables, it requires a physical parameterisation or closure.

### 198 2.3 Predictive Algorithm: Convolutional Neural Networks

199 Convolutional Neural Networks (CNNs) have proven successful in many areas of  
 200 computer vision [Krizhevsky et al., 2012; Simonyan and Zisserman, 2014; Dong et al.,  
 201 2016], where the primary objective is to extract information from an image, in order to  
 202 perform a particular task. CNNs work by applying successive layers of convolutions (a  
 203 form of spatial filtering) to the input; the complexity of the extracted information in-  
 204 creases with the number of convolution layers. The powerful property of CNNs is that  
 205 the filters of each convolution are learnt as part of the training process - they are not spec-  
 206 ified a priori. Therefore CNNs learn to extract the most ‘useful’ information from the  
 207 input variable, given training on a particular dataset.

208 We chose to use CNNs, as opposed to a deep neural network of multiple fully-connected  
 209 layers, due to their superior performance in computer vision tasks where the inputs have  
 210 a two dimensional structure [Krizhevsky et al., 2012]. We wanted a machine learning al-  
 211 gorithm that could exploit the two dimensional lateral structure of turbulent fluids. Spa-  
 212 tial filtering of the equations of motion of turbulent fluids is not new, and is used in Large  
 213 Eddy Simulation (LES) [Moeng, 1984; Sagaut, 2006]. Therefore, the learnt-filtering op-  
 214 erations of a CNN appeared to be a natural choice of data-driven algorithm to apply to  
 215 geophysical flows.

216 The training process involves the minimisation of an appropriately defined loss func-  
 217 tion, which measures the difference between the output of the CNN, and the desired tar-  
 218 gets. If the optimisation procedure was successful, such that the loss function on pre-  
 219 viously unseen data converges, the CNN will have learnt to extract the most important  
 220 information from the input. The CNN then uses the information to predict continuous  
 221 values. The CNN constructs the final prediction through a linear regression layer, which  
 222 regresses the desired output onto the final feature maps (feature maps are the interme-  
 223 diate results of each convolution layer).

224 Here we use CNNs to represent the sub-filter eddy momentum forcing. The input  
 225 is the filtered-streamfunction  $\bar{\psi}$  of the upper vertical layer, which represents our resolved  
 226 variable that the neural networks will extract information from. The output variables  
 227 are the zonal  $S_x$  and meridional  $S_y$  components of the sub-filter momentum forcing  $\mathbf{S}$ ,  
 228 defined by Equation 8. An example input and output is shown in Figure 1. Separate CNNs  
 229 are trained for each component of the sub-filter momentum forcing  $S_x$  and  $S_y$ . We only  
 230 consider data from the upper-layer of the model; this is because the flow is surface-intensified,  
 231 and we are assuming that our filtered quantities are similar to satellite altimetry data,  
 232 which only provide information at the surface.

233 In addition to testing whether it is possible to train a neural network to predict  
 234  $S_x$  and  $S_y$ , from  $\bar{\psi}$ , we explore how a neural network trained on one region performs on  
 235 another previously unseen region, i.e. how important local vs non-local information is  
 236 for different regions. We therefore construct three different datasets from the QG model  
 237 data, one for each region being studied. We choose regions which differ most in their dy-  
 238 namical behaviour, and are shown in Figure 1a: Region 1 is near the jet-separation point  
 239 of the western boundary, where there is a strong, inertial zonal jet. Region 2 is near the  
 240 eastern boundary downstream of the jet extension, where the dynamics are more wave-  
 241 like in nature. Region 3 is in the centre of the southern gyre, which is energetically less  
 242 active than regions 1 and 2.

243 Data from the three regions are split temporally into training and validation datasets.  
 244 The 10-years of daily data (3650 days) are split into the first  $\sim 9$  years (3300 days) to  
 245 train the neural networks, and the final year (350 days) is set aside for validation. To  
 246 reduce the computational cost, and the number of parameters of each CNN, we split each  
 247 region spatially from the initial  $160 \times 160$  grid points, to sixteen  $40 \times 40$  grid point sub-  
 248 regions, as depicted in Figure 1c. Reducing the input and output size of the neural net-  
 249 work from  $160 \times 160$  to  $40 \times 40$  significantly decreases the number of trainable weights,  
 250 and therefore the computational cost (we attempted to make predictions for the full  $160 \times 160$   
 251 of each training region, but this led to a neural network with over 250,000,000 param-  
 252 eters, which was computationally impractical).

253 Making predictions for a  $40 \times 40$  area instead of a  $160 \times 160$  area also increases the  
 254 amount of training and validation data by a factor of sixteen, from 3300 and 350 sam-  
 255 ples, to 52800 and 5600 respectively, where a sample is defined as a single input-output  
 256 pair of the neural network. We therefore have 52800 spatial maps (size  $40 \times 40$  grid points)  
 257 of input-output pairs to train the neural networks, and 5600 spatial maps of input-output  
 258 pairs set aside for validation.

259 We train CNNs to separately predict  $S_x$  and  $S_y$ , using data from three different  
 260 regions of the model; this gives a total of 6 neural networks. Each neural network is de-  
 261 noted by  $f_i(\bar{\psi}, \mathbf{w}_R)$ , where  $i = (x, y)$  refers to the component of  $\mathbf{S}$  being predicted,  $\mathbf{w}_R$   
 262 are the trained weights of the neural network, and  $R = 1, 2, 3$  refers to the region on  
 263 which the neural network has been trained. For example, the neural network trained on  
 264 region 2 to predict the meridional component  $S_y$  is denoted by  $f_y(\bar{\psi}, \mathbf{w}_2)$ .

To distinguish predictions from the true values, we label neural network predictions  
 as  $\tilde{S}_x = f_x(\bar{\psi}, \mathbf{w}_R)$ , and  $\tilde{S}_y = f_y(\bar{\psi}, \mathbf{w}_R)$ , while the true values of the sub-filter mo-  
 mentum forcing remain as  $S_x, S_y$ . We use the mean-squared error as the loss function,

$$L = \sum (S_x - \tilde{S}_x)^2, \text{ or } \sum (S_y - \tilde{S}_y)^2, \quad (9)$$

265 which quantifies the difference between the neural network predictions and the truth,  
 266 and where the summation is over all samples. The neural networks are trained (i.e. opti-  
 267 mised) using a form of stochastic gradient descent, namely the Adam optimisation al-  
 268 gorithm [Kingma and Ba, 2014], which minimises the loss function  $L$  defined in Equa-  
 269 tion 9. The training of each neural network  $f_i(\bar{\psi}, \mathbf{w}_R)$ , iteratively adjusts the values of  
 270 the weights  $\mathbf{w}_R$ , such that the loss function in Equation 9 is minimised. Therefore each  
 271 neural network has a different set of weights  $\mathbf{w}_R$ ; it is these weights which determine how  
 272 each neural network extracts information and makes predictions.

273 The architecture used for each  $f_i(\bar{\psi}, \mathbf{w}_R)$  contains three convolution layers, a max  
 274 pooling layer, and a final fully-connected layer (Figure 1). The max pooling layer reduces  
 275 the dimensionality of the previous layer, by selecting the maximum value within a  $2 \times 2$   
 276 grid point area - max pooling is effective when there is significant correlation between  
 277 points in the feature maps. To give the neural networks the ability to learn non-linear  
 278 functions, activation functions are added between layers. Here we use the scaled expo-  
 279 nential linear unit (SELU) [Klambauer et al., 2017]. SELU activation functions scale the



280 data towards zero mean and unit variance, removing the need for batch normalisation  
 281 - batch normalisation enforces zero mean and unit variance at each stage of the network,  
 282 but requires additional training.

283 The specific architecture was constructed by adjusting all parameters and observ-  
 284 ing which configuration most effectively minimises the loss function on the validation data.  
 285 See Table 1 for more details of the architecture and training procedure. The total num-  
 286 ber of parameters of each neural network is 325,728.

287 We train and implement each neural network using Keras [Chollet et al., 2015], with  
 288 the Tensorflow backend [Abadi et al., 2016]. Before training, all datasets are separately  
 289 normalised to zero mean and unit variance. Each CNN is trained for 200 epochs (1 epoch  
 290 = 1 full pass of all the training data through the optimisation algorithm), taking approx-  
 291 imately 10 CPU hours, after which there is negligible change in the loss function of the  
 292 validation data.

293 Once all six neural networks are trained, we make the predictions  $\tilde{S}_x$  and  $\tilde{S}_y$  us-  
 294 ing the filtered-stream function  $\bar{\psi}$  from the validation dataset, i.e., the final year of with-  
 295 held data. We make predictions for the full-domain to determine how each neural net-  
 296 work generalises to unseen, dynamically-distinct, regions. As the input and output size  
 297 of each neural network is  $40 \times 40$  grid points, we tile together predictions for the full do-  
 298 main of size  $512 \times 512$ ; the tiling leads to errors at the boundaries of each tile, where dis-  
 299 continuities can emerge. To reduce the tiling error, we make predictions using overlap-  
 300 ping tiles, and then average the results at each grid point.

301 In order to make predictions of the sub-surface flow field, using only information  
 302 at the surface, we train a new neural networks. The new neural network has an iden-  
 303 tical architecture to those discussed previously, and is trained to predict the middle-layer  
 304 streamfunction using the upper-layer streamfunction as the input; this neural network  
 305 is described in more detail in Section 6.

### 306 3 Neural Network Sensitivity and Generalisation

#### 307 3.1 Non-Local Predictions

308 The filtered streamfunction represents for example observational measurements from  
 309 satellite altimetry or coarse-resolution model data. The sub-filter eddy momentum forc-  
 310 ing represents unresolved turbulent processes. Our goal is to replicate the complex spatio-  
 311 temporal variability of  $S_x$  and  $S_y$  using neural networks  $f_i(\bar{\psi}, \mathbf{w}_R)$ . However observa-  
 312 tional data such as moorings [Hogg, 1992] or gliders [Rudnick et al., 2004; Davis et al.,  
 313 2008], may only be available for a particular region; we therefore only train the neural  
 314 networks using data from specific regions of the full domain, as described in Section 2.3.  
 315 Our aims are to both successfully train the neural networks, and to study how they gen-  
 316 eralise to previously un-seen regions.

317 We study the spatio-temporal variability of  $S_x$  and  $\tilde{S}_x$ , by examining snapshots,  
 318 the time-mean, and the standard deviation, shown in Figure 2. Diagnostics are calcu-  
 319 lated over the full  $512 \times 512$  domain, using the final year of withheld data. Both the spa-  
 320 tial and temporal variability of the true  $S_x$  are dominated by the jet dynamics (Figure 2a, e, and i).  
 321 In particular, strong meanders which extend eastward from the western boundary are  
 322 visible. The amplitude of the spatio-temporal variability of  $S_x$  ( $1.4 \times 10^{-6} \text{ms}^{-2}$ ) is of sim-  
 323 ilar magnitude to the time-mean ( $1.5 \times 10^{-6} \text{ms}^{-2}$ ).

324 All neural networks trained on three different regions, shown in Figure 1a and de-  
 325 scribed in Section 2.3, successfully reproduce the spatial patterns of the true  $S_x$ , as shown  
 326 by snapshots of the predictions  $\tilde{S}_x$  (Figure 2b, c, and d). Their magnitudes however vary  
 327 significantly. The predictions of  $f_x(\bar{\psi}, \mathbf{w}_1)$ , trained on data from the western boundary,



328 are almost identical to the true  $S_x$ , and successfully reproduces the correct amplitude  
 329 and variability (Figure 2b, f, j). The neural network  $f_x(\bar{\psi}, \mathbf{w}_2)$ , trained on data from the  
 330 eastern boundary, underestimates the magnitude of the true  $S_x$  by approximately 50%,  
 331 despite reproducing the correct spatial patterns. The predictions of  $f_x(\bar{\psi}, \mathbf{w}_3)$ , trained  
 332 on the southern gyre, underestimates the true  $S_x$  by an order of magnitude (Figure 2d,  
 333 h, l).

334 As the variability of  $S_x$  is dominated by the jet, it is difficult to assess the accu-  
 335 racy of the neural network predictions  $\tilde{S}_x$  in quiescent regions such as the eastern bound-  
 336 ary or within the gyres. We therefore calculate the Pearson correlation, a dimensionless  
 337 quantity, between the true  $S_x$  and the predictions  $\tilde{S}_x$ . The predictions of  $f_x(\bar{\psi}, \mathbf{w}_1)$  and  
 338  $f_x(\bar{\psi}, \mathbf{w}_2)$  are highly correlated with the truth ( $r > 0.9$ ) within the jet, but tend towards  
 339 zero or negative correlation near the eastern boundary (Figure 2m and 2n). The predic-  
 340 tions of  $f_x(\bar{\psi}, \mathbf{w}_3)$  have a more consistent positive correlation across the gyres and other  
 341 more quiescent regions, (Figure 2o).

342 We observe similar results for the spatial and temporal variability of  $S_y$ , shown in  
 343 Figure 3: the variability within the jet dominates, with an amplitude ( $1 \times 10^{-6} \text{ms}^{-2}$ )  
 344 similar to  $S_x$ . The meandering of the jet again produces complex spatial patterns in  $S_y$ ,  
 345 which when averaged in time, produce a distinct sign change moving across the jet lat-  
 346 itudinally. For the predictions  $\tilde{S}_y$ , the neural network trained on the western boundary,  
 347  $f_y(\bar{\psi}, \mathbf{w}_1)$ , most effectively reproduces the true  $S_y$ . However, the time-mean of  $f_y(\bar{\psi}, \mathbf{w}_1)$   
 348 (Figure 3f) has a positive bias everywhere in the domain, whereas the time-means of  $f_y(\bar{\psi}, \mathbf{w}_2)$   
 349 and  $f_y(\bar{\psi}, \mathbf{w}_3)$  (Figure 3g and 3h respectively) do not.

350 The correlations between  $S_y$  and  $\tilde{S}_y$  are similar to the zonal component:  $f_y(\bar{\psi}, \mathbf{w}_1)$   
 351 and  $f_y(\bar{\psi}, \mathbf{w}_2)$  are highly correlated ( $r > 0.8$ ) within the jet, but not in the gyres. Where  
 352 as  $f_y(\bar{\psi}, \mathbf{w}_3)$  has a consistently positive correlation across the full domain, despite fail-  
 353 ing to reproduce the amplitude within the jet. In fact, the correlation of  $f_y(\bar{\psi}, \mathbf{w}_3)$  within  
 354 the jet (Figure 3o) is negative ( $r \approx -0.3$ ). The negative correlation implies that the  
 355 dynamical processes occurring within region 3, the southern gyre, have an opposite ef-  
 356 fect to the eddy momentum forcing occurring within region 1. The opposing effects of  
 357 eddies could be an example of regional variation in eddy forcing, as in *Waterman and*  
 358 *Jayne* [2010], who found that whether eddies were driving the large-scale flow or not,  
 359 depended critically on along-stream position.

360 Across all neural networks, the correlation decreases at the eastern boundary, which  
 361 is partly caused by the sub-filter momentum forcing being orders of magnitude lower than  
 362 elsewhere in the domain. The low magnitude of  $S_x$  and  $S_y$  is due to the wave-like be-  
 363 haviour of the flow having a larger spatial-scale. The larger spatial-scale at the eastern  
 364 boundary leads to little variability at small scales, reducing the eddy momentum forc-  
 365 ing to almost zero, and therefore causing the performance of neural networks to deter-  
 366 iorate.

367 Overall, we see that training neural networks on the western boundary is most suc-  
 368 cessful when generalising to other areas of the domain (in terms of correlations and re-  
 369 producing the variability). Training on the eastern boundary produced good correlations  
 370 in the western boundary, but underestimated the magnitude of the eddy forcing by ap-  
 371 proximately 50%. Training on the southern gyre did not correlate well within the west-  
 372 ern boundary, and underestimated the truth by an order of magnitude.

373 Hence to successfully reproduce the correct amplitude and variability across the  
 374 domain, the training data must contain a diverse range of scale interactions, which here  
 375 corresponds to training on the most turbulent region. However, training on the turbu-  
 376 lent regions can lead to significant net biases in the predictions, as seen in Figure 3f. How  
 377 to correct for such biases will be discussed in Section 5.

378

### 3.2 Generalising to Different Reynolds Numbers

379

380

381

382

383

384

385

386

387

In Section 3.1, we investigated how neural networks trained on different regions of the domain generalise to other previously unseen regions. We now test how the neural networks generalise to different regimes, in particular different Reynolds number. In Section 3.1, we found that the neural networks trained on region 1, the western boundary, successfully generalised to different regions; we therefore apply  $f_x(\bar{\psi}, \mathbf{w}_1)$  to new model data with different wind stress amplitudes and viscosity coefficients to test its performance. We use models with higher and lower wind forcings, to test regimes which are both more and less turbulent than the original model, which had a wind stress amplitude of  $\tau_0 = 0.8 \text{ Nm}^{-2}$  and viscosity  $\nu = 75 \text{ m}^2\text{s}^{-2}$ .

388

389

390

391

392

We use the low-pass on filter the upper-layer streamfunction from each different model run, with the following:  $\nu = 200 \text{ m}^2\text{s}^{-2}$ , and  $\tau_0 = 0.3, 0.6$ , and  $0.9 \text{ Nm}^{-2}$ , and then apply the already-trained neural network  $f_x(\bar{\psi}, \mathbf{w}_1)$  to generate predictions  $\tilde{S}_x$ . The standard deviation of the true  $S_x$ , the standard deviation of the  $f_x(\bar{\psi}, \mathbf{w}_1)$  predictions  $\tilde{S}_x$ , and the correlation between them, are shown in Figure 4.

393

394

395

396

397

398

399

400

401

The neural network  $f_x(\bar{\psi}, \mathbf{w}_1)$  reproduces the variability within the jet almost exactly, across all runs, as can be seen by comparing the standard deviations in the first and second columns, which represent the standard deviation of the true  $S_x$  and predicted  $\tilde{S}_x$  respectively. The correlation within the jet remains high ( $r > 0.9$ ) in all runs, including the model with an increased wind forcing ( $\tau_0 = 0.9 \text{ Nm}^{-2}$ ) in Figure 4o. The correlations weaken at the eastern boundary for the lowest wind forcing ( $\tau_0 = 0.3 \text{ Nm}^{-2}$ ), shown in Figure 4f; this may be caused by an increase in the wave-like behaviour at the eastern boundary, which is not well captured by the neural networks. In general, the higher the Reynolds number, the better the correlations, i.e., more dark red areas of  $r > 0.8$ .

402

403

404

The mean biases of the predictions of the new models are similar in magnitude to the biases of the original model configuration. These biases showed no relationship with the Reynolds number, and are therefore not discussed further.

405

## 4 Sensitivity of Neural Networks to Under-Sampling

406

407

408

409

410

411

412

413

414

415

We have so far trained the neural networks with densely sampled data, i.e., we have data at each grid point for both the input and output variables. However, most observational datasets are spatially sparse, e.g. Argo floats [Roemmich *et al.*, 2009]. We therefore explore the impact of under-sampling with a new collection of neural networks trained on region 1 to predict  $S_x$ , but with the training data sub-sampled. At each time-slice of the training data, we randomly sample (without replacement)  $N$  points of the  $40 \times 40$  input variables,  $\bar{\psi}$ , and output variables  $S_x$ . Using these  $N$  randomly sampled values, we use a cubic interpolation to reconstruct the full  $40 \times 40$  grid point input and output (with a nearest-neighbour interpolation for grid points that fall outside the convex hull of the cubic interpolation).

416

417

418

419

420

421

422

These reconstructed time-slices from sub-sampled data are used to train a new set of neural networks. We vary the number of points  $N$  sub-sampled from  $> 90\%$  to  $< 5\%$  of the original 1600 points of the input and output variables. We have a neural network for each value of  $N$ , the sub-sampling rate. Using the neural networks trained on under-sampled data, we calculate the root-mean square error (RMSE) on the final year of validation data over the entire domain. The validation data is not sub-sampled, providing a stronger and more accurate test of the neural networks performance.

423

424

425

426

The RMSE is shown as a function of percentage of points sampled (Figure 7c). We find that the RMSE increases significantly only when the percentage of spatial points sampled drops below 10% (the error doubles at a sub-sampling rate of 4.7%). Note that the RMSE is not a monotonic function of percentage of points sampled due to the stochas-

427 tic nature of the training procedure and the use of a non-linear interpolation. The spa-  
 428 tial map of RMSE of the neural network trained with 18.75% sub-sampled data (Fig-  
 429 ure 7b) shows minimal changes relative to the neural network trained on the original (un-  
 430 altered) training data (Figure 7a). The result further suggests that the use of sparse in-  
 431 terpolated observations can be successfully used to accurately train and predict the eddy  
 432 momentum forcing as shown in Sections 3.1 and 3.2.

433 We also tested an alternative method of under-sampling, where the  $40 \times 40$  input  
 434 and output grid of the neural network is spaced out over the entire domain. In other words,  
 435 we sub-sample the input and output variables of the original  $512 \times 512$  grid to a regularly  
 436 spaced  $40 \times 40$  grid. However, training a convolutional neural network with this method-  
 437 ology did not work and led to severe overfitting (i.e. increasing validation loss during train-  
 438 ing). The neural networks presented in Section 2 learn to take first and second order deriva-  
 439 tives of the input streamfunction (see GitHub repository), which correspond to the ve-  
 440 locities and velocity shears. Both velocities and velocity shears are important features  
 441 to provide for accurate predictions of the eddy momentum forcing. By severely sub-sampling  
 442 the input streamfunction, the local information relevant to estimate velocities and ve-  
 443 locity shears is lost.

## 444 5 Physically-Constrained Neural Networks

445 We proceed to examine the net input of momentum from the neural network pre-  
 446 dictions  $\tilde{S}_x$  and  $\tilde{S}_y$ , which should vanish. If neural networks are used to leverage the use  
 447 of observational datasets and coarse-resolution models, then spurious sources of momen-  
 448 tum would violate physical conservation laws. We therefore need to constrain the neu-  
 449 ral networks to respect the physical properties of the system. Here we diagnose the mo-  
 450 mentum biases of the neural networks  $f_i(\bar{\psi}, \mathbf{w}_R)$ , and then explore different methods of  
 451 imposing conservation of momentum globally.

### 452 5.1 Momentum Biases

453 Each sub-region (including those used to train the neural networks) may have a  
 454 non-zero spatially-integrated momentum tendency. However, globally, the true sub-filter  
 455 momentum forcing  $\mathbf{S}$  should re-distribute momentum, and not act as a source or sink,  
 456 i.e.  $\iint \mathbf{S} dx dy = 0$ . We therefore need the neural networks to not introduce spurious  
 457 sources of momentum, to respect the physical properties of the system. By training each  
 458 neural network on a sub-region, we expect to have imperfect momentum conservation,  
 459 which will depend upon the particular dynamical processes within each region. For ex-  
 460 ample, if eddies within a particular region are driving the mean-flow, then we would ex-  
 461 pect a positive source of momentum locally - a neural network trained on such a region  
 462 would likely generalise the (local) input of momentum to the rest of the domain. A net  
 463 source or sink of momentum will manifest as a non-zero bias after spatial averaging.

464 At a single point in space, the time series of the predictions  $\tilde{S}_x$  and  $\tilde{S}_y$  show that  
 465 the neural networks trained on regions 1 and 2 track the true  $S_x$  and  $S_y$  closely (Fig-  
 466 ure 5a and 5b), reproducing a significant proportion ( $> 80\%$ ) of the variance. However,  
 467 if at each time-step we spatially average the neural network predictions  $\tilde{S}_x$  and  $\tilde{S}_y$  (Fig-  
 468 ure 5c and 5d respectively) over the full domain, we observe significant non-zero biases.

469 Consider the zonal component of the eddy momentum forcing in Figure 5c:  $f_x(\bar{\psi}, \mathbf{w}_1)$   
 470 has a net positive bias, implying a global positive increase of zonal momentum at all times,  
 471 while both  $f_x(\bar{\psi}, \mathbf{w}_2)$  and  $f_x(\bar{\psi}, \mathbf{w}_3)$  have negative biases, indicating a net decrease in  
 472 zonal momentum. We can estimate the magnitude of the resulting change in zonal ve-  
 473 locity from these net biases, over a period of a year, by assuming  $\Delta u = \langle \tilde{S}_x \rangle \Delta t$ , where  
 474  $\langle \rangle$  denotes the spatial average over the full domain. For  $f_x(\bar{\psi}, \mathbf{w}_1)$ ,  $f_x(\bar{\psi}, \mathbf{w}_2)$ , and  $f_x(\bar{\psi}, \mathbf{w}_3)$ ,  
 475 we obtain values of  $\langle \tilde{S}_x \rangle = 0.03, 0.02$ , and  $0.0008$  ( $10^{-6} \text{ms}^{-2}$ ) respectively; this leads

476 to zonal velocity changes of  $\Delta u = 0.95, 0.63,$  and  $0.025$  ( $\text{ms}^{-1}$ ). These changes are of  
 477 similar magnitude to the time-mean zonal flow, which peaks at approximately  $0.9 \text{ ms}^{-1}$   
 478 within the jet core.

479 There are also significant biases in the predictions of the meridional component  $\tilde{S}_y$ ,  
 480 shown in Figure 5d. The positive bias of  $f_y(\bar{\psi}, \mathbf{w}_1)$  is visible in the time-mean  $\tilde{S}_y$  shown  
 481 in Figure 3f. We can again estimate the change in meridional velocities by assuming  $\Delta v =$   
 482  $\langle \tilde{S}_y \rangle \Delta t$ . Using values of  $\langle \tilde{S}_y \rangle = 0.02, -0.01,$  and  $0.002$  ( $10^{-6} \text{ms}^{-2}$ ) for  $f_y(\bar{\psi}, \mathbf{w}_1), f_y(\bar{\psi}, \mathbf{w}_2),$   
 483 and  $f_y(\bar{\psi}, \mathbf{w}_3)$  respectively, leads to the following changes:  $\Delta v = 0.63, -0.31,$  and  $0.06$  ( $\text{ms}^{-1}$ ).  
 484 Some of these changes are the same magnitude as the time-mean meridional flow.

## 485 5.2 Towards Momentum-Conserving Neural Networks

486 The predictions of neural networks  $f_x(\bar{\psi}, \mathbf{w}_1)$  and  $f_y(\bar{\psi}, \mathbf{w}_1)$ , described in Section 3.1,  
 487 correctly reproduce the correct amplitude and variability of the true eddy momentum  
 488 forcing  $S_x$  and  $S_y$ , as seen in Figures 2 and 3. However, training on region 1 also pro-  
 489 duced some of the largest non-zero biases in  $\tilde{S}_x$  and  $\tilde{S}_y$  after spatial averaging at each  
 490 time step. We therefore test whether we can reduce the biases when training on region  
 491 1, while preserving the accuracy of predictions from the neural network. We trial three  
 492 approaches (A, B, and C) to reduce the biases identified in Figure 5c and 5d.

- 493 (A) Architecture Alteration: Train neural networks on region 1, but with the final fully-  
 494 connected layer modified such that the spatial mean is removed from the final out-  
 495 put. The neural networks will therefore be trained to reproduce the sub-filter mo-  
 496 mentum forcing, but with momentum conservation intrinsically embedded. I.e. same  
 497 training data, but altered architecture. The motivation behind this approach is  
 498 that if the local source of momentum within the  $40 \times 40$  output grid is zero, then  
 499 this may reduce the global net source of momentum.
- 500 (B) Pre-processing of input: Train on region 1 with the original architecture described  
 501 in Table 1 but with the spatial-mean removed at each snapshot within the train-  
 502 ing data. I.e. enforce momentum conservation in the training data, but make no  
 503 changes to the architecture. If the local source of momentum of each  $40 \times 40$  out-  
 504 put grid is zero within the training data, then the neural network may move to-  
 505 wards local momentum conservation during training. Though this does not guar-  
 506 antee that subsequent predictions will have zero local bias.
- 507 (C) Post-processing of output: train on region 1, and enforce global momentum con-  
 508 servation after the predictions have been made. I.e. no changes to training data  
 509 or architecture, but with additional processing of the full-domain predictions  $\tilde{S}_x$  and  $\tilde{S}_y$ .

510 The associated neural networks of each approach are labelled as  $f_i(\bar{\psi}, \mathbf{w}_1^A), f_i(\bar{\psi}, \mathbf{w}_1^B),$   
 511 and  $f_i(\bar{\psi}, \mathbf{w}_1^C)$  respectively, where  $i = (x, y)$  denotes either the zonal  $S_x$  or meridional  
 512  $S_y$  component being predicted.

513 All neural networks are optimised using the same training parameters given in Ta-  
 514 ble 1. Approach A, which alters the architecture, and approach B, which alters the train-  
 515 ing data, are enforcing momentum conservation not just globally, but within the  $40 \times 40$   
 516 sub-region being predicted. This local conservation is useful for enforcing global conser-  
 517 vation. However local conservation may not be desirable if there's convergence of eddy  
 518 momentum fluxes in a particular region, which can impact the large-scale flow, e.g. if  
 519 eddies are fluxing momentum into the jet at a particular along-stream position, enforc-  
 520 ing local conservation in a neural network may lead to missing these effects. Therefore  
 521 caution must be taken with restricting architectures in this way.

522 We now explore the performance of the newly constrained neural networks and the  
 523 net momentum input relative to that of the original neural networks trained on region

524 1:  $f_x(\bar{\psi}, \mathbf{w}_1)$  and  $f_y(\bar{\psi}, \mathbf{w}_1)$ . The spatial-averages of neural networks based on approaches  
525 A, B, and C are shown in Figure 6, with the same scale axes as in Figure 5.

526 Approach B has significant biases of approximately -0.01 and -0.015 ( $10^{-6}\text{ms}^{-2}$ )  
527 in the zonal and meridional components respectively; the optimisation procedure aims  
528 to reproduce the *variability* in the training data, and not spatial-means, therefore pre-  
529 processing the training data does not remove the biases. Compared to the original neu-  
530 ral networks trained on region 1, the biases of approaches A and C are 3 to 5 orders of  
531 magnitude lower, in both the zonal and meridional components. The post-processing ap-  
532 proach is exactly zero by construction, while the altered-architecture approach A is not  
533 exactly zero due to the overlapping-tiling procedure. The biases of  $f_x(\bar{\psi}, \mathbf{w}_1^A)$  and  $f_y(\bar{\psi}, \mathbf{w}_1^A)$   
534 are approximately -0.002 and -0.0005 ( $10^{-6}\text{ms}^{-2}$ ) which, over the course of a year, would  
535 lead to velocity changes of  $\Delta u = -0.06$  and  $\Delta v = -0.01$  ( $\text{ms}^{-1}$ ) respectively - now an  
536 order of magnitude smaller than the time-mean flow.

537 The correlation maps of all momentum-conserving approaches (not shown) change  
538 little from the original correlation maps of  $f_x(\bar{\psi}, \mathbf{w}_1)$  and  $f_y(\bar{\psi}, \mathbf{w}_1)$ , shown in Figure 2m and 3m  
539 respectively. All approaches reproduce the correct spatial patterns of the true  $S_y$  and  
540  $S_y$  (e.g., Figure 6 for standard deviations). However, approaches A and B underestimate  
541 the amplitude of  $S_x$  and  $S_y$  by approximately 20-30%, whereas there is a little difference  
542 between approach C and the truth ( $< 10\%$ ).

543 In summary, approach C of post-processing successfully enforces momentum con-  
544 servation, without sacrificing accuracy in the predictions of the eddy momentum momen-  
545 tum forcing. Approach B, altering the training data, was not efficacious at reducing the  
546 net biases. The physically-constrained architecture of approach A successfully reduced  
547 the net bias, but at the expense of 20-30% accuracy. Though further altering of the archi-  
548 tecture (e.g. increasing number of convolution layers and filters) or training proce-  
549 dure (decreasing the learning rate, with increased number of training epochs) could re-  
550 duce this drop in accuracy by countering the restriction placed on the architecture.

## 551 6 Predicting Sub-Surface Flow

552 We have shown that neural networks, by using the filtered-streamfunction as the  
553 input variable, can provide information on unresolved turbulent processes, namely the  
554 sub-filter momentum forcing. We have assumed that the filtered-streamfunction repre-  
555 sents some limited set of observations, or data from a coarse-resolution ocean model. How-  
556 ever, coarse-resolution ocean models still produce data for below the surface, whereas  
557 satellite observations do not. Here we address the issue of inferring sub-surface informa-  
558 tion solely from surface fields. Our approach is conceptually similar to *Chapman and Cha-*  
559 *rantonis* [2017], which used a form of neural network called a self-organising map to re-  
560 construct sub-surface velocities in the Southern ocean, using satellite altimetry and Argo  
561 float data. Using the QG model data described in Section 2.1, we test whether a neu-  
562 ral network can predict the middle-layer streamfunction, using only the surface filtered-  
563 streamfunction.

564 We train a new neural network  $\tilde{\psi}_2 = f(\bar{\psi}_1, \mathbf{W})$  (which has the same architecture  
565 as before, but with a different output and weights) to minimise the mean-squared error  
566 loss function  $L \propto (\psi_2 - \tilde{\psi}_2)^2$ , where  $\bar{\psi}_1$  is the filtered-streamfunction of the upper-layer,  
567  $\psi_2$  is the true streamfunction of the middle-layer, and  $\tilde{\psi}_2$  is the neural network predic-  
568 tions. Again, to assess the ability to generalise to unseen regions, we only train the neu-  
569 ral network on the western boundary (training region 1). Diagnostics of the true  $\psi_2$  and  
570 predictions  $\tilde{\psi}_2$ , including the correlation between them, are shown in Figure 8a-e. The  
571 neural network accurately reproduces the middle-layer time-mean and standard devia-  
572 tion of the streamfunction within the jet region. The neural network accurately repro-  
573 duces the correct amplitude of the true  $\psi_2$  within the jet, but underestimates the am-



574 plitude by  $\approx 50\%$  within the gyres. Independent of the amplitude, the predictions  $\tilde{\psi}_2$  are  
 575 highly correlated ( $r > 0.8$ ) almost everywhere in the domain with the true  $\psi_2$ .

576 The decrease in accuracy in the gyres is likely due to only training within the west-  
 577 ern boundary, where the streamfunctions of the upper- and middle-layers are more tightly  
 578 coupled due to the strong barotropic nature of the flow. Within the gyres, the barotropic  
 579 component is not as dominant - this could cause the neural networks to underestimate  
 580 the amplitude away from the jet. Alternatively the adjustment time scales of the upper-  
 581 and middle-layers are not the same, which perhaps requires more training data in order  
 582 to capture interactions over longer time scales.

583 We take the approach one step further, by predicting the bottom-layer streamfunc-  
 584 tion, using the same neural network and its weights  $f(\bar{\psi}_1, \mathbf{W})$ , but now using the pre-  
 585 dictions of the middle-layer streamfunction as the input, i.e.,  $\tilde{\psi}_3 = f(\tilde{\psi}_2, \mathbf{W})$ . We test  
 586 whether a neural network trained to predict the middle-layer streamfunction can pro-  
 587 vide any information on the bottom-layer streamfunction (without re-training), by in-  
 588 putting the middle-layer streamfunction as an input. Mathematically, this is written as  
 589  $\tilde{\psi}_3 = f(f(\bar{\psi}_1, \mathbf{W}), \mathbf{W})$ .

590 Diagnostics of the true ( $\psi_3$ ) and predicted ( $\tilde{\psi}_3$ ) bottom-layer streamfunction are  
 591 shown in Figure 8f-j. Despite a moderate correlation of  $r \approx 0.5$  across the domain, the  
 592 predictions fail to reproduce the correct time-mean, which has a circulation in the op-  
 593 posite direction to the truth. This is due to the neural network being trained to predict  
 594 the middle-layer flow, which on average is more aligned with the upper-layer. Therefore  
 595 when the neural network is given the middle-layer streamfunction as an input, it pre-  
 596 dicted the bottom-layer flow as on-average being in the same direction, which is not the  
 597 case. The neural network also hasn't be trained to predict the effects of the additional  
 598 bottom drag, decreasing the accuracy further - more data could improve this issue, as  
 599 the longer time scales associated with bottom drag may be absent from the training dataset.

600 An alternative approach would be to train a new neural network to map directly  
 601 from the surface flow to the bottom-layer flow, i.e.,  $\tilde{\psi}_3 = f(\bar{\psi}_1, \mathbf{W})$ . Having separate neu-  
 602 ral networks for the middle- and bottom-layers, you could then reconstruct the flow at  
 603 all depths using just information at the surface (although an additional neural network  
 604 does increase computational costs). Independent of the abyssal flow however, we have  
 605 shown that neural networks can provide information on the flow at intermediate depths.

## 606 7 Conclusions & Discussion

### 607 7.1 Summary

608 In this study, we have demonstrated as a proof-of-concept that machine learning  
 609 algorithms can provide information on unresolved turbulent processes, when given a smoothed-  
 610 view of the dynamics (i.e. the filtered-streamfunction). We degrade data from a high-  
 611 resolution eddy-resolving QG model using a spatial low-pass filter, and train convolu-  
 612 tional neural networks to predict the relationship between turbulent processes and their  
 613 effect on the large-scale flow, i.e. the eddy momentum forcing. Our results show that con-  
 614 volutional neural networks can successfully represent both the spatial and temporal vari-  
 615 ability of the eddy momentum forcing.

616 We determine how neural networks trained on one area of the domain, perform in  
 617 other previously-unseen areas (Figures 2 and 3), representing when observational data  
 618 is limited to only particular regions, for example mooring data [Hogg, 1992] or gliders  
 619 [Rudnick et al., 2004; Davis et al., 2008]. Training on a sub-region tests the sensitivity  
 620 of the neural network performance to the underlying physical processes. We find that  
 621 the region on which the neural network is trained significantly impacts the accuracy, as  
 622 well as the mean-bias which impacts momentum conservation. In particular, training on



623 the least energetically active region, the southern gyre, leads to the lowest accuracy; these  
 624 neural networks could not reproduce the variability in more energetic regions, such as  
 625 within the meandering jet. However, training on the western boundary leads to the best  
 626 generalisation, in terms of reproducing the correct amplitude of the eddy momentum forc-  
 627 ing in the rest of the domain.

628 The variation in performance between regions implies that training on the most  
 629 turbulent region leads to the best performing neural networks for eddy momentum forc-  
 630 ing prediction. It is possible that data from the most turbulent regions exhibits the high-  
 631 est variance, or contains a more diverse range of scale-interactions. However, two regions  
 632 may be as turbulent or energetically active as each other, but the nature of the eddy-  
 633 mean flow interactions within them may differ. For example, *Waterman and Jayne* [2010]  
 634 showed that in an idealised model the effect of eddies on the mean-flow depended crit-  
 635 ically on along-stream position: up-stream eddies are generated by an unstable jet, while  
 636 down-stream the eddies drive the time-mean circulation. Therefore training neural net-  
 637 works on different along-stream positions may lead to different dynamical-processes be-  
 638 ing learnt, despite both regions being energetically active. Here we have shown how the  
 639 performance varies between regions of differing energetic activity, but how the specific  
 640 effects of eddies- e.g. driving the mean-flow, versus eddies extracting momentum and en-  
 641 ergy from the jet -impacts the neural network performance remains to be determined.

642 Without further training, we show that a neural network trained on one QG model  
 643 configuration generalises exceedingly well to QG models with different viscosity coeffi-  
 644 cients and wind forcings (Figure 4). The neural network within the jet reproduces the  
 645 correct spatio-temporal variability (<10% error) in all configurations, and the more tur-  
 646 bulent the configuration, the better the correlation between the predicted  $\tilde{S}_x$  and the true  
 647  $S_x$  within the gyres. While the neural networks do not conserve momentum globally (Fig-  
 648 ure 5c and 5d), we show that momentum conservation can be enforced without a sig-  
 649 nificant reduction in accuracy (Figure 6), through either a physically-constrained archi-  
 650 tecture or post-processing of the predictions.

651 We also show that a new neural network can be trained to predict the middle-layer  
 652 streamfunction, using only the upper-layer streamfunction as the input, i.e., predicting  
 653 the flow at depth using information at the surface (Figure 8). The highest accuracy oc-  
 654 curs where the barotropic component of the flow is most dominant, which coincides with  
 655 a strong zonal mean-flow. However, when using the streamfunction to predict the bottom-  
 656 layer streamfunction, the neural network captures some of the variability, but fails to repli-  
 657 cate the time-mean of the true bottom-layer streamfunction  $\psi_3$  (Figure 8), primarily due  
 658 to the presence of bottom-drag.

## 659 7.2 Implications for leveraging observations

660 Our work has implications for inference from sparse observations. While previous  
 661 studies have used machine learning to leverage observational datasets [*Chapman and Cha-*  
 662 *rantonis*, 2017; *Su et al.*, 2018; *Giglio et al.*, 2018], the present work demonstrates that  
 663 convolutional neural networks in particular are an excellent tool for such tasks. Neural  
 664 networks should be further tested and exploited in the future for data inference due to

- 665 • their resilience, such that accurate predictions for the full domain can be gener-  
 666 ated by training on a sub-region.
- 667 • their generalisation to different external forcings, without any further training such  
 668 that predictions outside the regime trained on can be successful.
- 669 • their ability to be successfully trained with under-sampled data. (Figure 7).

670 Collectively, these results suggest that sparse interpolated observational datasets  
 671 can be leveraged by such data-driven techniques. For example, satellite altimetry data

672 can be used to predict the sub-surface flow; or data from moorings deployed in Drake  
 673 Passage as part of the Diapycnal and Isopycnal Mixing Experiment in the Southern Ocean  
 674 (DIMES) can be used to infer eddy momentum or heat flux divergences in other parts  
 675 of the Southern Ocean. In addition, datasets from Argo floats [*Chapman and Sallée, 2017*],  
 676 mooring data, ADCPs, and SSH from altimetry, could be combined to reconstruct physically-  
 677 and biogeochemically important quantities such energy reservoirs, or air-sea fluxes, in-  
 678 terior transport and/or storage of heat, carbon and oxygen in the ocean [*Su et al., 2018*;  
 679 *Giglio et al., 2018*].

### 680 7.3 Implications for parametrizations

681 Although we have motivated our study through the leverage of observations and  
 682 coarse-resolution model data, our results have implications for eddy parameterisations  
 683 of momentum, and more generally for sub-grid parametrizations. As discussed previously,  
 684 machine learning has been used to parameterise unresolved processes in the atmosphere  
 685 [*Brenowitz and Bretherton, 2018*; *Jiang et al., 2018*; *Gentine et al., 2018*; *O’Gorman and*  
 686 *Dwyer, 2018*]. We have shown that neural networks can successfully represent the spatio-  
 687 temporal variability of the eddy momentum forcing, implying potential for data-driven  
 688 oceanic turbulence closures in the future. The generalisation ability of the neural net-  
 689 works shows that only a limited amount of observations or high-resolution model data  
 690 may be needed to successfully represent sub-grid scale processes. While the CNNs are  
 691 successful at representing relationship between the eddy momentum forcing and their  
 692 effect on the resolved flow, the low-resolution climate models might have biases that are  
 693 too severe (e.g., weak transport and velocity shears) to lead to a successful representa-  
 694 tion of the eddy momentum forcing from CNNs as trained here. Yet, our results also show  
 695 that they perform very well for different forcing and dissipation terms, therefore until  
 696 the CNNs are implemented into a coarse-resolution ocean model, their success in improv-  
 697 ing numerical simulations is purely speculative but deserves to be investigated.

698 Whether neural networks are being used to leverage observations, or more impor-  
 699 tantly to construct a data-driven eddy parameterisation, caution must be taken to en-  
 700 sure that the laws of physics are respected. More work into physically-constrained ma-  
 701 chine learning algorithms is crucial, and successful applications of data-driven techniques  
 702 should incorporate physical knowledge. Indeed, the neural network turbulence model of  
 703 *Ling et al.* [2016b] out-performed more simple linear models only when Galilean invari-  
 704 ant stress tensors from *Pope* [1975] were used, which are also a key ingredient of the eddy  
 705 parameterisation proposed by *Anstey and Zanna* [2017]. As previously discussed, we suc-  
 706 cessfully enforce global momentum conservation in the present work, such that future  
 707 implementations of data-driven parameterisations, despite being semi-empirical, can be  
 708 altered to respect physical principles. Specifically, physical constraints can be incorpo-  
 709 rated into the architecture of the predictive algorithms.

710 One disadvantage of convolutional neural networks is the computational cost of the  
 711 matrix operations of each convolution layer to make a prediction given an input. The  
 712 total time complexity (ignoring any fully-connected layers) of a CNN [*He and Sun, 2015*]  
 713 is given by  $\mathcal{O}(\sum_l^d n_{l-1} \cdot s_l^2 \cdot n_l \cdot m_l^2)$ , where  $d$  is the total number of convolution layers,  $l$   
 714 is the index of a convolution layer,  $n_l$  is the number of filters,  $s_l$  is the filter size, and  $m_l$   
 715 is the size of the output feature map. The time complexity is larger than that of a tra-  
 716 ditional eddy closure (e.g., a simple laplacian dissipation of momentum which only in-  
 717 volves a few matrix additions and subtractions). One way to reduce the time complex-  
 718 ity is to instead use depth-wise separable convolution layers [*Howard et al., 2017, e.g*],  
 719 which treat the input channels of a convolution layer more independently. This reduces  
 720 the number of parameters and hence computational cost. An alternative way of reduc-  
 721 ing time complexity is to simply reduce the sizes of the input and outputs, i.e. make pre-  
 722 dictions for a region smaller than  $40 \times 40$  grid points. The amount of information avail-  
 723 able to make predictions is therefore reduced. The computational cost is an area which

needs addressing if CNNs are to be routinely implemented in models in the future. However, unlike other parametrizations, the training of the neural networks is only done once.

#### 7.4 Future Work

Our study is a step towards using convolutional neural networks to extend the reach of currently available observational or model data. Our proof-of-concept study was conducted in an idealised QG model. The next stage involves training neural networks on actual observational datasets (as described in Section 7.2) or on more realistic model data (e.g. a 1/40th degree global model which resolves the mesoscale and submesoscale eddy fields, such as in *Rocha et al.* [2016]).

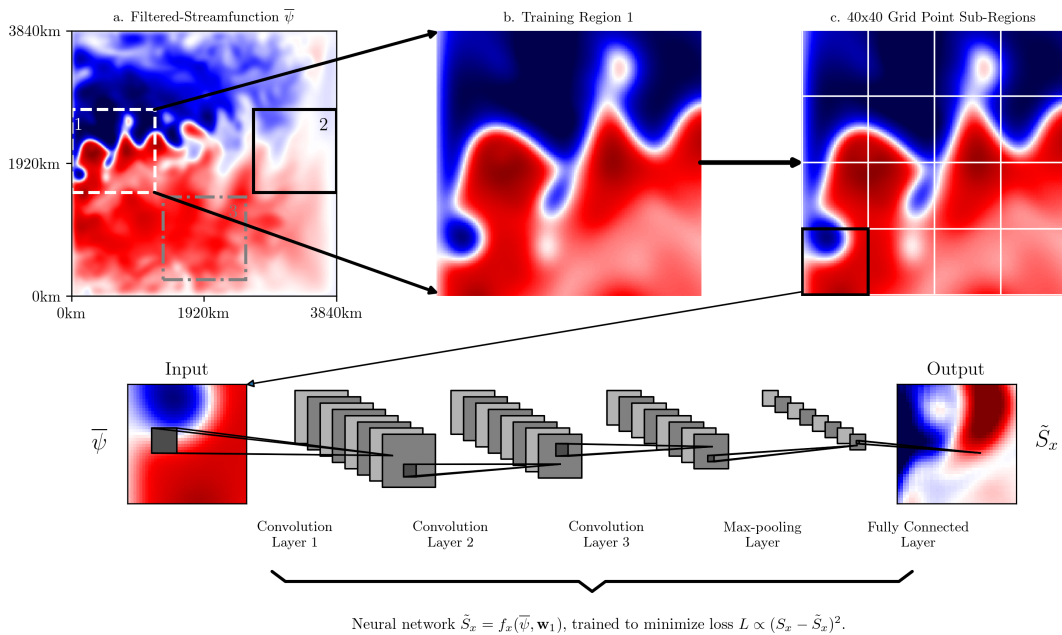
We used nine years of data to train the neural networks, and one year for validation. *Gentine et al.* [2018] showed, with regards to parameterising convection with neural networks, that the training dataset could be reduced in size from 12 months to 3 months, with little change in the overall mean-squared error. The sensitivity our neural networks to reductions in the amount of training data needs to be systematically explored. We have only determined the impact of spatial under-sampling on the neural networks. However, further work is needed to determine the impact of using a few number of time-slices (e.g. using 3 years of training data as opposed to 9 years used here).

Training on the western boundary produces the best performance. However, the high skill within the jet does not fully translate to high skill in all parts of the gyres. The best correlations in the gyres occurs instead when training on the southern gyre, and not the western or eastern boundaries (Figure 2 and 3). This implies there may be an optimal combination of the predictions of the neural networks trained on different regions, in order to produce the best overall generalisation and potentially include non-local effects. E.g., each neural network has a weight  $a_i$ , and the optimal predictions for the full domain is a combination of all neural networks

$$\tilde{S}_x^{OPT} = \sum_i^N a_i f_x(\bar{\psi}, \mathbf{w}_i), \quad (10)$$

where the summation is over all regions, and  $\tilde{S}_x^{OPT}$  is the corresponding optimal prediction (with an analogous  $\tilde{S}_y^{OPT}$  for the meridional component). Combining predictions from multiple neural networks in this manner could be a useful way of capturing the distinct eddy-mean flow interactions observed by *Waterman and Jayne* [2010]. Alternatively, if the computational resources are available, you could train a single neural network on data from all three regions, in the hope that it ‘remembers’ the physical processes occurring in each region. The risk with this approach is that one loses specialisation, and the skill reduces as the single neural network simply ‘averages’ the effects of the three regions together. We will attempt to implement the neural networks (as trained here, or as a combination of neural networks) into a coarse resolution version of the QG model to test their performance as a sub-grid scale parametrization.

Although this study is a proof-of-concept, the merging of data-driven methods with physical knowledge has the potential to change the way the physics of the ocean are studied in the future. The combination of physical theory and machine learning could prove more effective than either component in isolation.



764 **Figure 1.** Panel (a) illustrates the upper-layer filtered-streamfunction  $\bar{\psi}$  of the QG model,  
 765 including the three regions in which we train the neural networks: region 1 (white-dashed)  
 766 is on the western boundary, region 2 (black-solid) is on the eastern boundary, and region 3  
 767 (grey-dash-dotted) is centered on the southern gyre. Panel (b) shows a close-up of the filtered-  
 768 streamfunction  $\bar{\psi}$  within training region 1 while Panel (c) illustrates how training region 1 is  
 769 split into 16  $40 \times 40$  grid point sub-regions - the size of the input and output arrays of the neural  
 770 network is  $40 \times 40$  grid points. The input variable of each neural network is the filtered stream-  
 771 function  $\bar{\psi}$ , and the output variable is either the zonal component  $\tilde{S}_x$  or meridional component  
 772  $\tilde{S}_y$  of the sub-filter eddy momentum forcing. The architecture of the convolutional neural net-  
 773 work, with an example input  $\bar{\psi}$  and output  $\tilde{S}_x$ , is illustrated underneath Panels (a), (b), and (c).

## 816 Acknowledgments

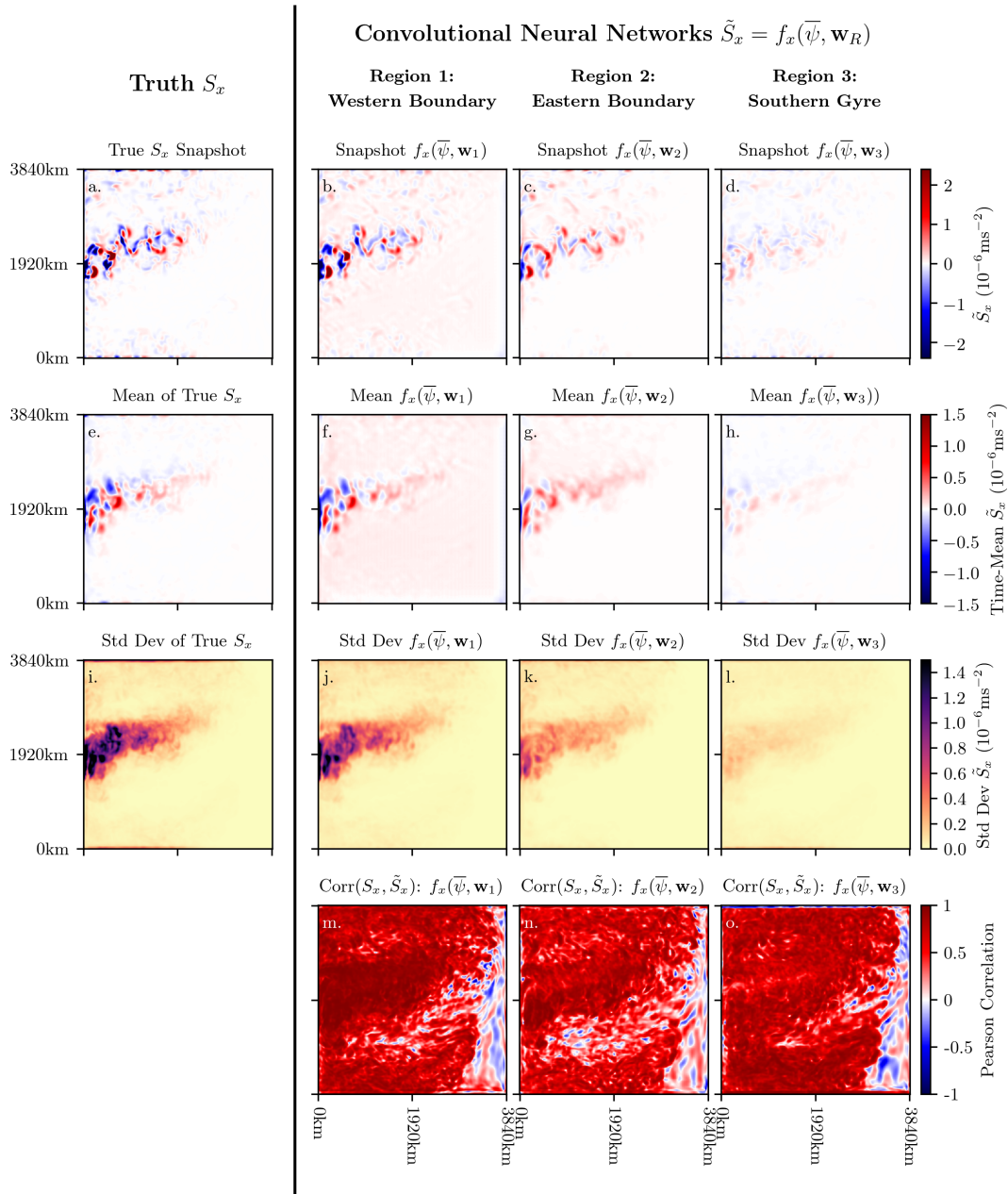
817 This study was funded by the Natural Environment Research Council (NERC). We thank  
 818 PierGianLuca Porta Mana, who conducted the high-resolution PEQUOD model simu-  
 819 lations. Thank you to Robert Fraser, Tomos David, and Ryan Abernathey for their help-  
 820 ful discussions during the development of this work, and to two anonymous reviewers  
 821 for their comments which helped improve this manuscript. The trained Keras neural net-  
 822 works, their training histories, and the Python code used to produce this paper, can all  
 823 be found in the following GitHub repository: <https://github.com/TomBolton/DeepEddy>.

## 824 References

- 825 Abadi, M., P. Barham, J. Chen, Z. Chen, A. Davis, J. Dean, M. Devin, S. Ghe-  
 826 mawat, G. Irving, M. Isard, et al. (2016), Tensorflow: A system for large-scale  
 827 machine learning., in *OSDI*, vol. 16, pp. 265–283.
- 828 Abernathey, R. P., and J. Marshall (2013), Global surface eddy diffusivities derived  
 829 from satellite altimetry, *Journal of Geophysical Research: Oceans*, *118*(2), 901–  
 830 916.
- 831 Anderson, G. J., and D. D. Lucas (2018), Machine learning predictions of a multires-  
 832 olution climate model ensemble, *Geophysical Research Letters*, *45*(9), 4273–4280.

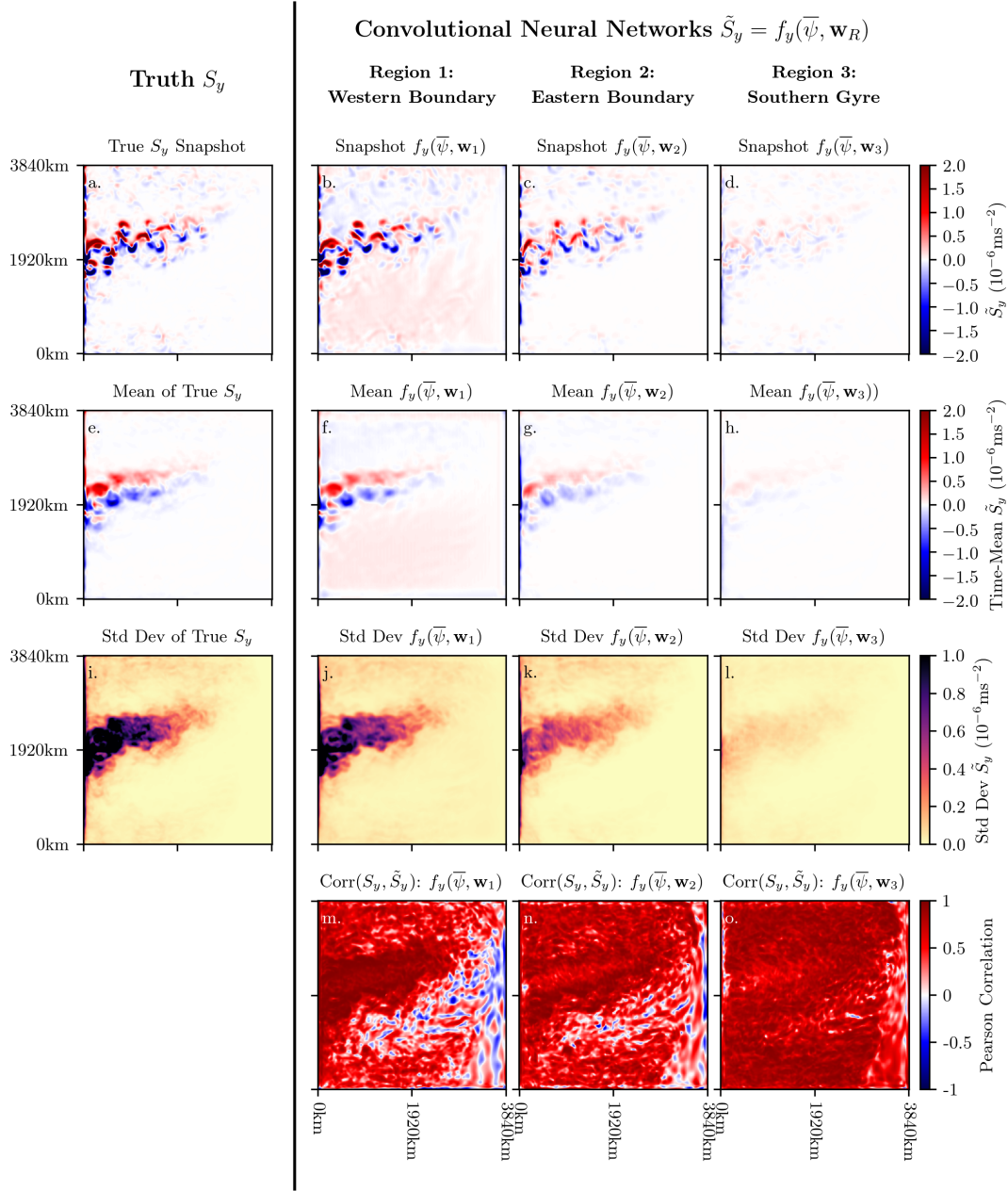
<b>Quasi-Geostrophic Model Parameters</b>	
Domain size (grid points)	512×512
Domain length ( $L$ )	3840 km
Resolution ( $\Delta x$ )	7.5 km
Viscosity ( $\nu$ )	75 m <sup>2</sup> s <sup>-1</sup>
Rosby deformation radii ( $L_{Ro}$ )	40,23 km
Velocity scale ( $\sqrt{EK\bar{E}}$ )	0.21 ms <sup>-1</sup>
Planetary vorticity ( $f_0$ )	10 <sup>-4</sup> s <sup>-1</sup>
Rosby parameter ( $\beta$ )	2 * 10 <sup>-11</sup> m <sup>-1</sup> s <sup>-1</sup>
Gravity ( $g$ )	9.8 ms <sup>-2</sup>
Reduced gravity ( $g'$ )	0.034, 0.018 ms <sup>-2</sup>
Bottom drag coefficient ( $r$ )	4 * 10 <sup>-8</sup> s <sup>-1</sup>
Wind stress amplitude ( $\tau_0$ )	0.8 Nm <sup>-2</sup>
Reference density ( $\rho_0$ )	10 <sup>3</sup> kgm <sup>-3</sup>
<b>Neural Network Data Details</b>	
Data source	Quasi-geostrophic ocean model
Input variable (feature)	Filtered streamfunction $\bar{\psi}$
Output variables (targets)	Sub-filter momentum forcing $S_x, S_y$
Training Region 1	Western boundary
Training Region 2	Eastern boundary
Training Region 3	Southern gyre
Number of training samples	52800 (years 1-9)
Number of validation samples	5600 (year 10)
Standardisation method	Zero mean, unit variance
<b>Neural Network Architecture</b>	
Input size	40×40
Number of convolution layers	3
Number of filters for each convolution layer	16, 16*8, 8*8
Size of filter for each convolution layer	8×8, 4×4, 4×4
Filter stride for each convolution layer	2, 1, 1
Activation function for each convolution layer	SELU, SELU, SELU
Max pooling kernel size	2
Output layer activation function	None/Linear
Output size	40×40
<b>Neural Network Training Parameters</b>	
Loss function	Mean-square error
Optimiser	Adam
Learning rate	0.001
Momentum	0.9
Batch size	16
Training epochs	200

774 **Table 1.** Details on the following: the quasi-geostrophic ocean model parameters, the datasets  
775 used to train the neural networks, the architecture parameters, and the optimisation parameters.

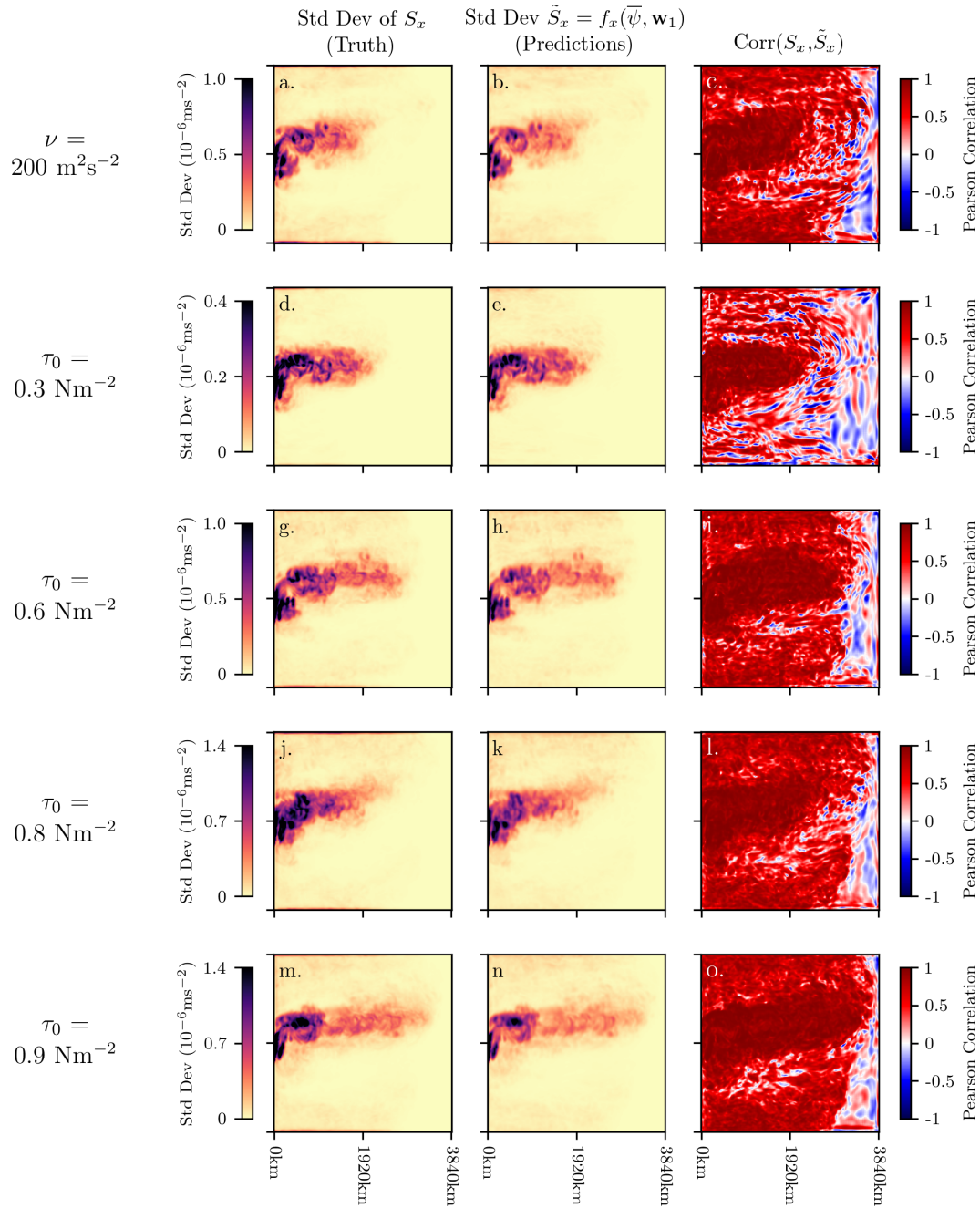


776 **Figure 2.** Examining the non-local prediction ability. Comparisons of the true zonal component of the sub-filter momentum forcing  $S_x$ , with the neural networks trained using data from  
 777 three different regions. The first three rows compare snapshots, time-means, and the standard  
 778 deviation respectively, while the bottom row shows the correlation between the true  $S_x$  and the  
 779 predictions  $\tilde{S}_x$ . The first column contains the diagnostics using the true zonal sub-filter momentum  
 780 forcing  $S_x$ , while columns two, three, and four use predictions  $\tilde{S}_x$  from the neural networks  
 781  $f_x(\bar{\psi}, \mathbf{w}_1)$ ,  $f_x(\bar{\psi}, \mathbf{w}_2)$ , and  $f_x(\bar{\psi}, \mathbf{w}_3)$  respectively. All diagnostics were produced using the validation  
 782 data.  
 783

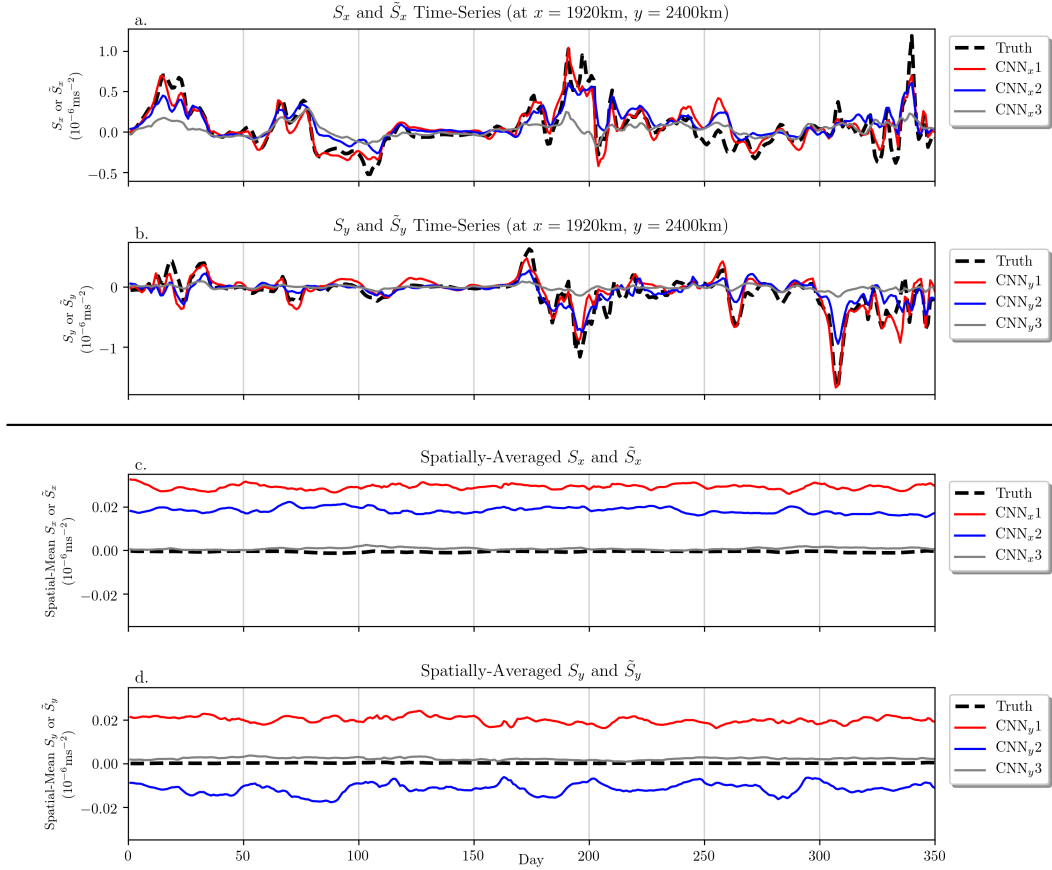




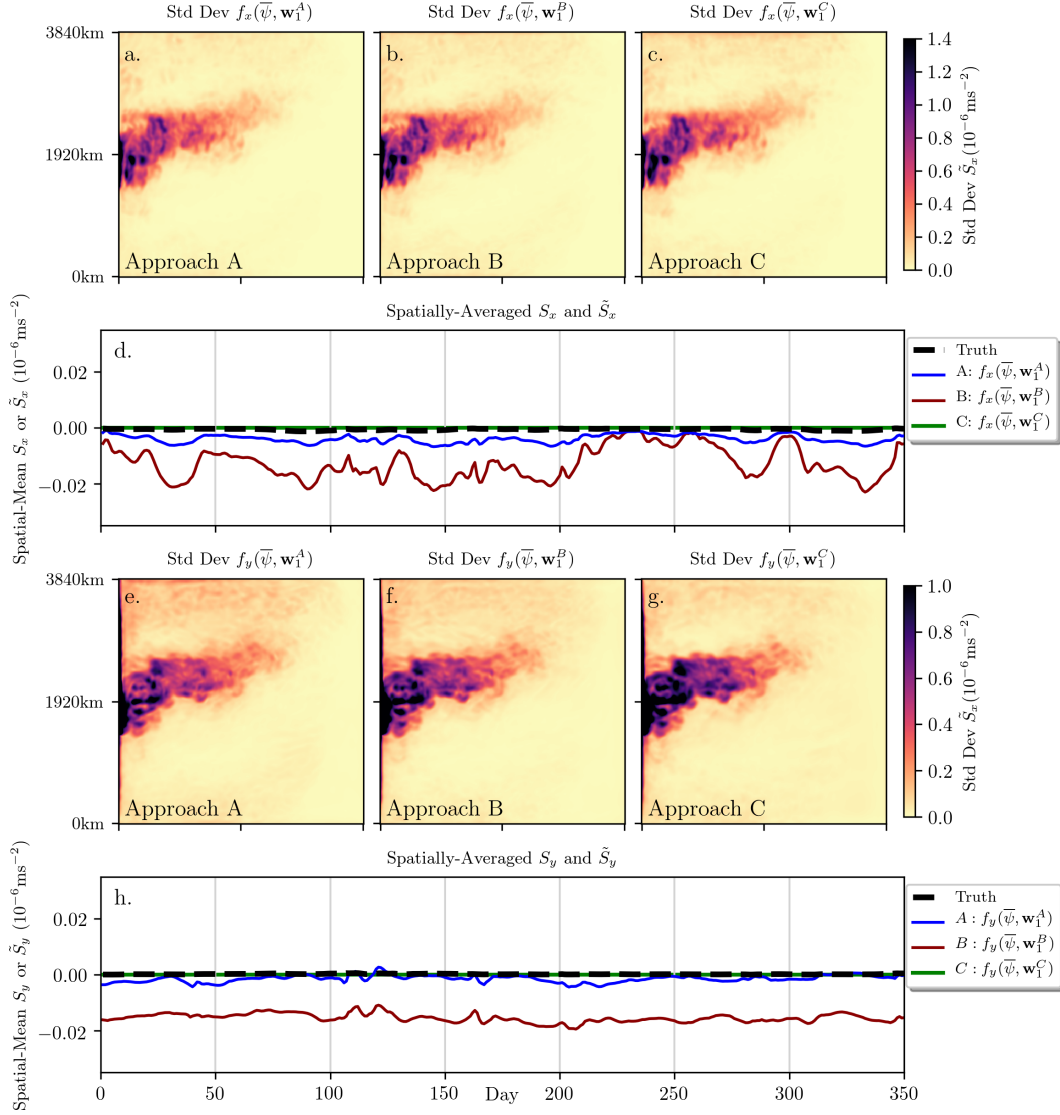
784 **Figure 3.** The same diagnostics as Figure 2, but for the meridional component of the sub-  
 785 filter momentum forcing: the true  $S_y$  and the predictions  $\tilde{S}_y$  from the neural networks  $f_y(\bar{\psi}, \mathbf{w}_1)$ ,  
 786  $f_y(\bar{\psi}, \mathbf{w}_2)$ , and  $f_y(\bar{\psi}, \mathbf{w}_3)$ .



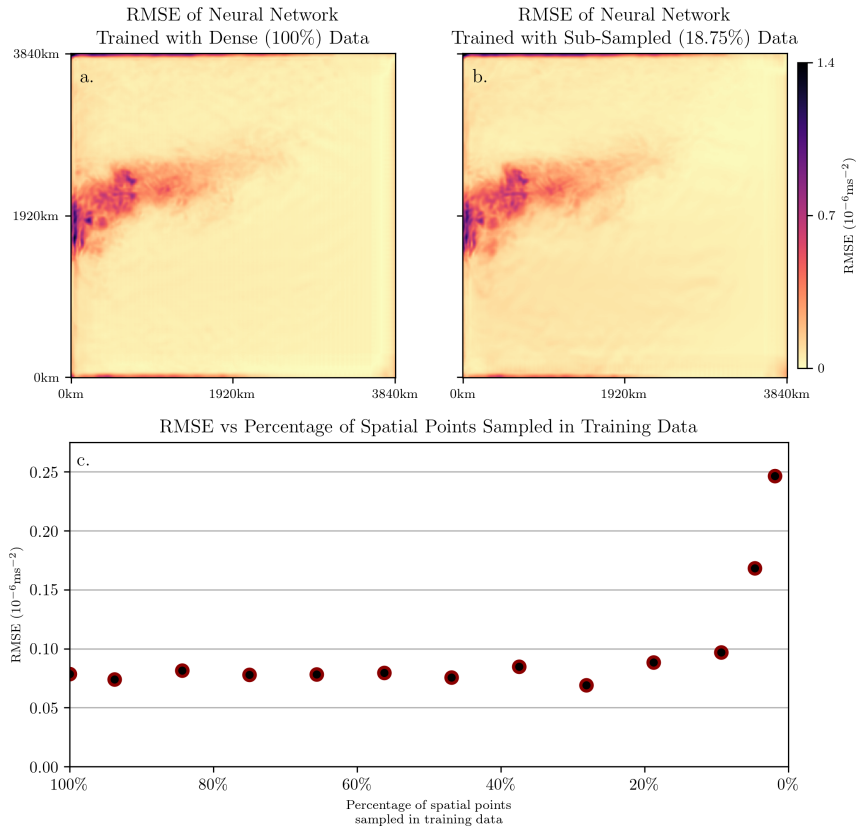
787 **Figure 4.** Examining the ability to generalise to new regimes: using the trained neural net-  
 788 work  $f_x(\bar{\psi}, \mathbf{w}_1)$ , we make predictions for model runs of different viscosities and wind forcings.  
 789 From each model run, we use one year of the upper-layer filtered streamfunction to generate  
 790 predictions  $\tilde{S}_x$  from  $f_x(\bar{\psi}, \mathbf{w}_1)$  to see how they compare to the true  $S_x$ . We study a run of higher  
 791 viscosity  $\nu = 200 \text{ m}^2\text{s}^{-2}$ , and runs with wind stress amplitude  $\tau_0 = 0.3, 0.6, 0.8,$  and  $0.9 \text{ Nm}^{-2}$ .  
 792 Note that  $f_x(\bar{\psi}, \mathbf{w}_1)$  was trained on a run with  $\nu = 75 \text{ m}^2\text{s}^{-2}$  and  $\tau_0 = 0.8 \text{ Nm}^{-2}$ , the standard  
 793 deviation and correlation maps of which are included again here in Panels (j), (k), and (l).



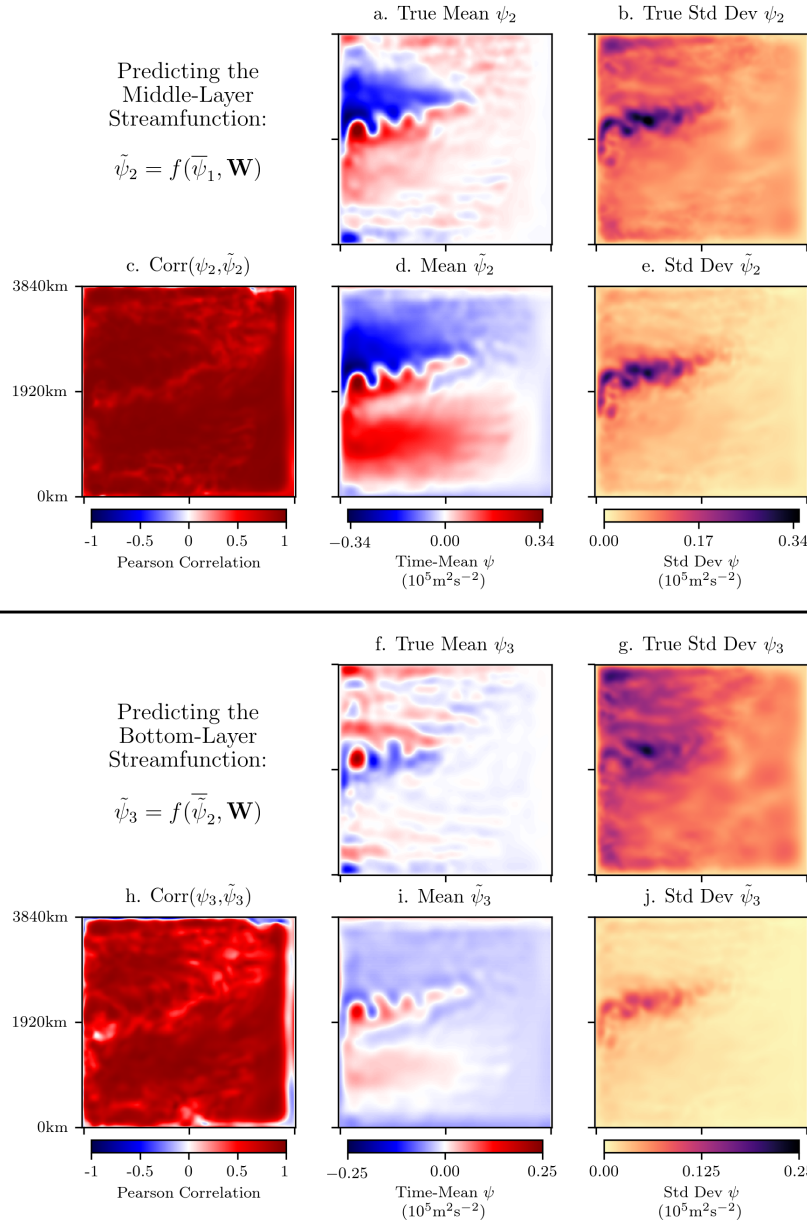
794 **Figure 5.** Panels (a) and (b) show time series of the zonal and meridional components of  
 795 the sub-filter momentum forcing respectively, at a single point near the middle of the domain.  
 796 Panels (c) and (d) also show time series of the zonal and meridional components of the sub-filter  
 797 momentum forcing, but this time spatially-averaged over the entire domain.



798 **Figure 6.** The standard deviation and spatial-average time series of the predictions  $\tilde{S}_x$  and  
 799  $\tilde{S}_y$  of the momentum conserving approaches A, B, and C. Panels (a), (b), and (c) show the  
 800 standard deviation of  $\tilde{S}_x$  from  $f_x(\bar{\psi}, \mathbf{w}_1^A)$ ,  $f_x(\bar{\psi}, \mathbf{w}_1^B)$ , and  $f_x(\bar{\psi}, \mathbf{w}_1^C)$  respectively, while Pan-  
 801 els (e), (f), and (g) show the standard deviation of  $\tilde{S}_y$  from  $f_y(\bar{\psi}, \mathbf{w}_1^A)$ ,  $f_y(\bar{\psi}, \mathbf{w}_1^B)$ , and  $f_y(\bar{\psi}, \mathbf{w}_1^C)$   
 802 respectively. The spatial-averages of these predictions  $\tilde{S}_x$  and  $\tilde{S}_y$  are shown in Panels (d) and (h).



803 **Figure 7.** Determining how under-sampling of the training data impacts neural network error.  
 804 Panel (a) shows the RMSE of the neural network  $f_x(\bar{\psi}, \mathbf{w}_1)$  trained with dense (un-altered)  
 805 training data, while Panel (b) shows the RMSE of the neural network trained with sub-sampled  
 806 (18.75%) data. Panel (c) shows the RMSE as a function of the percentage of spatial points  
 807 sampled at each time-slice of the training data. Note that the RMSE is calculated over the full-  
 808 domain during the validation period (the final year of data).



809 **Figure 8.** Predicting the middle- and bottom-layer streamfunctions  $\psi_2$  and  $\psi_3$  using the  
 810 upper-layer filtered streamfunction  $\bar{\psi}_1$ . We first train a new neural network to predict  $\psi_2$  from  
 811  $\bar{\psi}_1$ , i.e.,  $\psi_2 = f(\bar{\psi}_1, \mathbf{W})$ ; diagnostics of the true  $\psi_2$  and the predictions  $\tilde{\psi}_2$  are shown in the top-  
 812 half of the Figure. We then take the same neural network that was trained to predict  $\psi_2$  from  
 813  $\bar{\psi}_1$ , and now predict the bottom layer streamfunction  $\psi_3$  using the predicted middle-layer stream-  
 814 function as the input, i.e.,  $\psi_3 = f(\tilde{\psi}_2, \mathbf{W})$ ; the diagnostics of the true  $\psi_3$  and the predictions  $\tilde{\psi}_3$   
 815 are shown in the bottom-half of the Figure.



- 833 Anstey, J. A., and L. Zanna (2017), A deformation-based parametrization of ocean  
834 mesoscale eddy reynolds stresses, *Ocean Modelling*, *112*, 99–111.
- 835 Arbic, B. K., K. L. Polzin, R. B. Scott, J. G. Richman, and J. F. Shriver (2013), On  
836 eddy viscosity, energy cascades, and the horizontal resolution of gridded satellite  
837 altimeter products, *Journal of Physical Oceanography*, *43*(2), 283–300.
- 838 Berloff, P. S. (2005), On dynamically consistent eddy fluxes, *Dynamics of atmo-*  
839 *spheres and oceans*, *38*(3-4), 123–146.
- 840 Brenowitz, N. D., and C. S. Bretherton (2018), Prognostic validation of a neural  
841 network unified physics parameterization, *Geophysical Research Letters*.
- 842 Chapman, C., and A. A. Charantonis (2017), Reconstruction of subsurface velocities  
843 from satellite observations using iterative self-organizing maps, *IEEE Geoscience*  
844 *and Remote Sensing Letters*, *14*(5), 617–620.
- 845 Chapman, C., and J.-B. Sallée (2017), Can we reconstruct mean and eddy fluxes  
846 from argo floats?, *Ocean Modelling*, *120*, 83–100.
- 847 Chelton, D. B., M. G. Schlax, R. M. Samelson, and R. A. de Szoeke (2007), Global  
848 observations of large oceanic eddies, *Geophysical Research Letters*, *34*(15).
- 849 Chollet, F., et al. (2015), Keras, <https://keras.io>.
- 850 Davis, R. E., M. D. Ohman, D. L. Rudnick, and J. T. Sherman (2008), Glider  
851 surveillance of physics and biology in the southern california current system,  
852 *Limnology and Oceanography*, *53*(5part2), 2151–2168.
- 853 Dong, C., C. C. Loy, K. He, and X. Tang (2016), Image super-resolution using deep  
854 convolutional networks, *IEEE transactions on pattern analysis and machine intel-*  
855 *ligence*, *38*(2), 295–307.
- 856 Durand, M., L.-L. Fu, D. P. Lettenmaier, D. E. Alsdorf, E. Rodriguez, and  
857 D. Esteban-Fernandez (2010), The surface water and ocean topography mission:  
858 Observing terrestrial surface water and oceanic submesoscale eddies, *Proceedings*  
859 *of the IEEE*, *98*(5), 766–779.
- 860 Esteves, J. T., G. de Souza Rolim, and A. S. Ferrauo (2018), Rainfall prediction  
861 methodology with binary multilayer perceptron neural networks, *Climate Dynam-*  
862 *ics*, pp. 1–13.
- 863 Gentine, P., M. Pritchard, S. Rasp, G. Reinaudi, and G. Yacalis (2018), Could  
864 machine learning break the convection parameterization deadlock?, *Geophysical*  
865 *Research Letters*.
- 866 Giglio, D., V. Lyubchich, and M. Mazloff (2018), Estimating oxygen in the south-  
867 ern ocean using argo temperature and salinity, *Journal of Geophysical Research:*  
868 *Oceans*.
- 869 Goodfellow, I., Y. Bengio, A. Courville, and Y. Bengio (2016), *Deep learning*, vol. 1,  
870 MIT press Cambridge.
- 871 Greatbatch, R., X. Zhai, M. Claus, L. Czeschel, and W. Rath (2010a), Transport  
872 driven by eddy momentum fluxes in the gulf stream extension region, *Geophysical*  
873 *Research Letters*, *37*(24).
- 874 Greatbatch, R. J., X. Zhai, J.-D. Kohlmann, and L. Czeschel (2010b), Ocean eddy  
875 momentum fluxes at the latitudes of the gulf stream and the kuroshio extensions  
876 as revealed by satellite data, *Ocean Dynamics*, *60*(3), 617–628.
- 877 Hallberg, R. (2013), Using a resolution function to regulate parameterizations of  
878 oceanic mesoscale eddy effects, *Ocean Modelling*, *72*, 92–103.
- 879 He, K., and J. Sun (2015), Convolutional neural networks at constrained time cost,  
880 in *Proceedings of the IEEE conference on computer vision and pattern recognition*,  
881 pp. 5353–5360.
- 882 Hewitt, H. T., M. J. Roberts, P. Hyder, T. Graham, J. Rae, S. E. Belcher,  
883 R. Bourdallé-Badie, D. Copey, A. Coward, C. Guiavarch, et al. (2016), The  
884 impact of resolving the rossby radius at mid-latitudes in the ocean: Results from  
885 a high-resolution version of the met office gc2 coupled model, *Geoscientific Model*  
886 *Development*, *9*(10), 3655–3670.

- 887 Hogg, N. G. (1992), On the transport of the gulf stream between cape hatteras and  
 888 the grand banks, *Deep Sea Research Part A. Oceanographic Research Papers*,  
 889 *39*(7-8), 1231–1246.
- 890 Howard, A. G., M. Zhu, B. Chen, D. Kalenichenko, W. Wang, T. Weyand, M. An-  
 891 dreetto, and H. Adam (2017), Mobilenets: Efficient convolutional neural networks  
 892 for mobile vision applications, *arXiv preprint arXiv:1704.04861*.
- 893 Jiang, G.-Q., J. Xu, and J. Wei (2018), A deep-learning algorithm of neural network  
 894 for the parameterization of typhoon–ocean feedback in typhoon forecast models,  
 895 *Geophysical Research Letters*.
- 896 Jochum, M., G. Danabasoglu, M. Holland, Y.-O. Kwon, and W. Large (2008), Ocean  
 897 viscosity and climate, *Journal of Geophysical Research: Oceans*, *113*(C6).
- 898 Kang, D., and E. N. Curchitser (2015), Energetics of eddy–mean flow interactions in  
 899 the gulf stream region, *Journal of Physical Oceanography*, *45*(4), 1103–1120.
- 900 Keating, S. R., and K. S. Smith (2015), Upper ocean flow statistics estimated from  
 901 superresolved sea-surface temperature images, *Journal of Geophysical Research:*  
 902 *Oceans*, *120*(2), 1197–1214.
- 903 Keating, S. R., A. J. Majda, and K. S. Smith (2012), New methods for estimating  
 904 ocean eddy heat transport using satellite altimetry, *Monthly Weather Review*,  
 905 *140*(5), 1703–1722.
- 906 Kingma, D. P., and J. Ba (2014), Adam: A method for stochastic optimization,  
 907 *arXiv preprint arXiv:1412.6980*.
- 908 Kjellsson, J., and L. Zanna (2017), The impact of horizontal resolution on energy  
 909 transfers in global ocean models, *Fluids*, *2*(3), 45.
- 910 Klambauer, G., T. Unterthiner, A. Mayr, and S. Hochreiter (2017), Self-normalizing  
 911 neural networks, in *Advances in Neural Information Processing Systems*, pp. 972–  
 912 981.
- 913 Krizhevsky, A., I. Sutskever, and G. E. Hinton (2012), Imagenet classification with  
 914 deep convolutional neural networks, in *Advances in neural information processing*  
 915 *systems*, pp. 1097–1105.
- 916 Kutz, J. N. (2017), Deep learning in fluid dynamics, *Journal of Fluid Mechanics*,  
 917 *814*, 1–4.
- 918 Le Traon, P., and R. Morrow (2001), Ocean currents and eddies, in *International*  
 919 *Geophysics*, vol. 69, pp. 171–xi, Elsevier.
- 920 Le Traon, P., F. Nadal, and N. Ducet (1998), An improved mapping method of mul-  
 921 tisatellite altimeter data, *Journal of atmospheric and oceanic technology*, *15*(2),  
 922 522–534.
- 923 LeCun, Y., Y. Bengio, and G. Hinton (2015), Deep learning, *nature*, *521*(7553), 436.
- 924 Ling, J., R. Jones, and J. Templeton (2016a), Machine learning strategies for sys-  
 925 tems with invariance properties, *Journal of Computational Physics*, *318*, 22–35.
- 926 Ling, J., A. Kurzawski, and J. Templeton (2016b), Reynolds averaged turbulence  
 927 modelling using deep neural networks with embedded invariance, *Journal of Fluid*  
 928 *Mechanics*, *807*, 155–166.
- 929 Mana, P. P., and L. Zanna (2014), Toward a stochastic parameterization of ocean  
 930 mesoscale eddies, *Ocean Modelling*, *79*, 1–20.
- 931 McGovern, A., K. L. Elmore, D. J. Gagne, S. E. Haupt, C. D. Karstens,  
 932 R. Lagerquist, T. Smith, and J. K. Williams (2017), Using artificial intelligence  
 933 to improve real-time decision-making for high-impact weather, *Bulletin of the*  
 934 *American Meteorological Society*, *98*(10), 2073–2090.
- 935 Moeng, C.-H. (1984), A large-eddy-simulation model for the study of planetary  
 936 boundary-layer turbulence, *Journal of the Atmospheric Sciences*, *41*(13), 2052–  
 937 2062.
- 938 Morrow, R., R. Coleman, J. Church, and D. Chelton (1994), Surface eddy momen-  
 939 tum flux and velocity variances in the southern ocean from geosat altimetry,  
 940 *Journal of Physical Oceanography*, *24*(10), 2050–2071.

- 941 O’Gorman, P. A., and J. G. Dwyer (2018), Using machine learning to parameterize  
 942 moist convection: potential for modeling of climate, climate change and extreme  
 943 events, *Journal of Advances in Modelling Earth Systems*.
- 944 Pathak, J., B. Hunt, M. Girvan, Z. Lu, and E. Ott (2018a), Model-free prediction  
 945 of large spatiotemporally chaotic systems from data: a reservoir computing ap-  
 946 proach, *Physical review letters*, *120*(2), 024,102.
- 947 Pathak, J., A. Wikner, R. Fussell, S. Chandra, B. R. Hunt, M. Girvan, and E. Ott  
 948 (2018b), Hybrid forecasting of chaotic processes: using machine learning in con-  
 949 junction with a knowledge-based model, *Chaos: An Interdisciplinary Journal of*  
 950 *Nonlinear Science*, *28*(4), 041,101.
- 951 Pope, S. (1975), A more general effective-viscosity hypothesis, *Journal of Fluid*  
 952 *Mechanics*, *72*(2), 331–340.
- 953 Rocha, C. B., S. T. Gille, T. K. Chereskin, and D. Menemenlis (2016), Seasonality  
 954 of submesoscale dynamics in the kuroshio extension, *Geophysical Research Letters*,  
 955 *43*(21), 11–304.
- 956 Roemmich, D., G. C. Johnson, S. Riser, R. Davis, J. Gilson, W. B. Owens, S. L.  
 957 Garzoli, C. Schmid, and M. Ignaszewski (2009), The argo program: Observing the  
 958 global ocean with profiling floats, *Oceanography*, *22*(2), 34–43.
- 959 Rudnick, D. L., R. E. Davis, C. C. Eriksen, D. M. Fratantoni, and M. J. Perry  
 960 (2004), Underwater gliders for ocean research, *Marine Technology Society Journal*,  
 961 *38*(2), 73–84.
- 962 Sagaut, P. (2006), *Large eddy simulation for incompressible flows: an introduction*,  
 963 Springer Science & Business Media.
- 964 Scott, R. B., and F. Wang (2005), Direct evidence of an oceanic inverse kinetic en-  
 965 ergy cascade from satellite altimetry, *Journal of Physical Oceanography*, *35*(9),  
 966 1650–1666.
- 967 Simonyan, K., and A. Zisserman (2014), Very deep convolutional networks for large-  
 968 scale image recognition, *arXiv preprint arXiv:1409.1556*.
- 969 Su, H., W. Li, and X.-H. Yan (2018), Retrieving temperature anomaly in the global  
 970 subsurface and deeper ocean from satellite observations, *Journal of Geophysical*  
 971 *Research: Oceans*, *123*(1), 399–410.
- 972 Tracey, B. D., K. Duraisamy, and J. J. Alonso (2015), A machine learning strat-  
 973 egy to assist turbulence model development, in *53rd AIAA Aerospace Sciences*  
 974 *Meeting*, p. 1287.
- 975 Vlachas, P. R., W. Byeon, Z. Y. Wan, T. P. Sapsis, and P. Koumoutsakos (2018),  
 976 Data-driven forecasting of high-dimensional chaotic systems with long short-term  
 977 memory networks, *Proc. R. Soc. A*, *474*(2213), 20170,844.
- 978 Waterman, S., and S. R. Jayne (2010), Eddy-mean flow interactions in the along-  
 979 stream development of a western boundary current jet: An idealized model study,  
 980 *Journal of Physical Oceanography*.
- 981 Waterman, S., N. G. Hogg, and S. R. Jayne (2011), Eddy-mean flow interaction in  
 982 the kuroshio extension region, *Journal of Physical Oceanography*, *41*(6), 1182–  
 983 1208.
- 984 Zanna, L., P. P. Mana, J. Anstey, T. David, and T. Bolton (2017), Scale-aware de-  
 985 terministic and stochastic parametrizations of eddy-mean flow interaction, *Ocean*  
 986 *Modelling*, *111*, 66–80.